

AperTO - Archivio Istituzionale Open Access dell'Università di Torino

Treatment with ROS detoxifying gold clusters alleviates the progressive functional decline in a mouse model of Friedreich's Ataxia

This is the author's manuscript

Original Citation:

Availability:

This version is available <http://hdl.handle.net/2318/1815324> since 2021-11-01T10:38:40Z

Published version:

DOI:10.1126/scitranslmed.abe1633

Terms of use:

Open Access

Anyone can freely access the full text of works made available as "Open Access". Works made available under a Creative Commons license can be used according to the terms and conditions of said license. Use of all other works requires consent of the right holder (author or publisher) if not exempted from copyright protection by the applicable law.

(Article begins on next page)

**Treatment with ROS detoxifying gold clusters alleviates the progressive functional decline
in a mouse model of Friedreich's Ataxia**

Chiara Villa¹, Alessandro Umbach², Mariella Legato¹, Chiara Riganti³, Rebecca Jones², Beatrice Martini¹, Marina Boido⁴, Claudio Medana², Irene Facchinetti⁵, Dario Barni⁵, Milena Pinto⁶, Tania Arguello⁶, Marzia Belicchi¹, Gigliola Fagiolari⁷, Carla Liaci², Maurizio Moggio⁷, Riccardo Ruffo⁵, Carlos T. Moraes⁶, Angelo Monguzzi⁵, Giorgio R. Merlo², Yvan Torrente^{1,*}

¹Stem Cell Laboratory, Department of Pathophysiology and Transplantation, University of Milano, Milano, Fondazione IRCCS Ca' Granda Ospedale Maggiore Policlinico, Centro Dino Ferrari, via F. Sforza 35, 20122 Milano, Italy.

²Department of Molecular Biotechnology and Health Science, University of Torino, Via Nizza 52 10126 Torino, Italy.

³Department of Oncology, University of Turin, Via Santena 5/bis - 10126 Torino, Italy

⁴Neuroscience Institute Cavalieri Ottolenghi, Department of Neuroscience "Rita Levi Montalcini", University of Turin, Regione Gonzole 10, 10043 Orbassano (Torino), Italy.

⁵ Department of Material Science, University of Milano Bicocca, via R. Cozzi 55, 20125 Milano, Italy.

⁶Department of Neurology, University of Miami Miller School of Medicine, Miami, USA.

⁷ Neuromuscular and Rare Diseases Unit, Fondazione IRCCS Ca' Granda Ospedale Maggiore Policlinico, Milan, Italy.

*To whom correspondence should be addressed:

Yvan Torrente, Stem Cell Laboratory, Department of Pathophysiology and Transplantation, Università degli Studi di Milano, Unit of Neurology, Fondazione IRCCS Ca' Granda Ospedale Maggiore Policlinico, Centro Dino Ferrari, Milan, Italy yvan.torrente@unimi.it

Keywords: Friedreich's ataxia (FRDA), frataxin (FXN), gold clusters, autophagy, reactive oxygen species (ROS).

Abstract

Friedreich's ataxia (FRDA) is caused by the reduced expression of the mitochondrial protein frataxin (FXN) due to an intronic GAA trinucleotide repeat expansion in the *FXN* gene. Although FRDA has no cure and few treatment options, there is research dedicated to finding an agent that can curb disease progression and address symptoms as neurobehavioral deficits, muscle endurance and heart contractile dysfunctions. Since oxidative stress and mitochondrial dysfunction are implicated in FRDA, we demonstrated the systemic delivery of catalysts activity of gold cluster superstructures (Au_8 -pXs) to improve cell response to mitochondrial reactive oxygen species (ROS) and thereby alleviate FRDA-related pathology in mesenchymal stem cells of FRDA patients. We also found that systemic delivery of Au_8 -pXs induced significant amelioration of motor function and cardiac contractility of YG8sR mouse model that recapitulates the FRDA phenotypes. These effects were linked to long-term improvement of mitochondrial functions and antioxidant cell responses. We coupled these events with increased expression of frataxin, which is sustained by reduced autophagy. Overall, these results suggest a cascade of Au_8 -pXs-related signals that encourage further optimization of the use of Au_8 -pXs in experimental clinical strategies for the treatment of FRDA.

Introduction

Friedreich's ataxia (FRDA) is a multisystemic autosomal recessive disorder caused by a GAA repeat expansion mutation within intron 1 of the frataxin (*FXN*) gene (1, 2). Unaffected individuals have 5 to 40 GAA repeat sequences, whereas affected individuals have ~70 to more than 1000 GAA triplets (3). Long GAA repeats determines reduced expression of FXN, which is a highly conserved mitochondrial protein, involved in iron turnover, iron-sulfur cluster and heme biosynthesis (4, 5). Frataxin dysregulation is linked to dysfunction of the mitochondrial energy conversion and oxidative

phosphorylation (OXPHOS) through iron accumulation and increased production of reactive oxygen species (ROS), such as hydroxyl (HO[•]) and hydrogen peroxide (H₂O₂), leading to oxidative stress especially in mitochondria (6-9). Cellular antioxidant response is regulated by Nuclear factor E2-related factor 2 (Nrf2), a transcription factor that regulates cellular antioxidant response, inducing the expression of ROS-response antioxidant genes, by binding to the antioxidant response element (ARE) on nuclear DNA, including an ARE site within the FXN gene (10-13). In FRDA patients and mouse models, Nrf2 activity is compromised in response to oxidative insults, thus leading to reduced expression of antioxidant genes such as superoxide dismutase SOD-1 and -2 (12, 14, 15). Interestingly, Nrf2 expression correlates with frataxin gene expression (14). In addition to increased ROS production and loss of Nrf-2, frataxin deficiency is also associated with down-regulation of PGC-1 α , a master regulator of mitochondrial biogenesis (15, 16). The downregulation of PGC-1 α suggests early impairment of mitochondrial pathways as a potential mediator of mitochondrial loss and dysfunction in FRDA (17). Notably, another hallmark of FRDA is the imbalance of mitochondrial dynamics characterized by increased expression of the mitochondrial fusion protein mitofusin-1 (Mfn1) that triggers the formation of giant or larger disorganized mitochondria in rodent muscles (18) or in cultured cells (19-22). Autophagy is a key node for the regulation of ROS levels as well as for ROS-dependent cellular regulation. Autophagy comprises salvaging processes, commonly triggered by metabolic stress responses by which macromolecules and organelles such as mitochondria are targeted by autophagic vesicles to lysosomes for degradation and recycling of their constituents (23, 24). Among the plethora of signaling pathways regulating the interplay between ROS and autophagy, the mechanistic activation of Atg7-mediated conjugation of microtubule-associated protein 1 light chain 3 (LC3-I) to the membrane lipid phosphatidylethanolamine to form LC3-II interpret multiple cues, including oxidative stress, to integrate them with the control of energy management, anabolism, and cell growth (25, 26).

Several studies revealed that alterations in ROS and autophagy are implicated in FRDA (21). Indeed, imbalance of mitochondrial dynamics and autophagy has emerged as a common pathogenic element to several neurodegenerative diseases such as Parkinson's disease, Charcot-Marie-Tooth, Alzheimer's disease, Huntington's disease or amyotrophic lateral sclerosis (27, 28). Pathologically, frataxin insufficiency leads to spinocerebellar neurodegeneration, ataxia, muscle weakness, cardiomyopathy, diabetes mellitus and skeletal deformities (29-32). The transgenic YG8sR mouse model, which exclusively expresses two disease-causing human *FXN* transgenes (h*FXN*) containing GAA expansions, develops progressive neurological degeneration with locomotor and coordination deficits and muscle weakness by 3 months age (33). In addition, the YG8sR mice represent one of the most suitable and representative animal models of FRDA. Since no cure or effective treatment for FRDA has been reported, attempts to identify novel strategies to at least delay the disease progression are needed. Metal chelating agents able to target the excess of Fe^{3+} have been tested (34) with unsatisfactory results. Alternative antioxidant strategies exploit the use of coenzyme Q10 or CoQ10 analogues and derivatives (such as idebenone and mitoquinone) and vitamin E (35-37). Results from trials with these compounds indicate only partial efficacy. Another therapeutic approach for FRDA is epigenetic modulation through heterochromatin acetylation by histone deacetylase inhibitor (HDACi) to increase the mRNA and protein levels of *FXN* (38). Gene and stem cell therapy in animal and cell models showed some beneficial effect (39, 40). More recently, researchers used synthetic DNA or RNA or genome editing approaches to block R-loop formation, thereby triggering *FXN* gene activation to levels similar to wild-type cells (41-43). Here, we report a potential therapeutic strategy for FRDA that exploits gold quantum cluster ($\text{Au}_8\text{-pXs}$). $\text{Au}_8\text{-pXs}$ is a novel highly biocompatible material based on gold quantum clusters, i.e. sub-nanometer structures made from few units to hundred gold atoms, which possess excellent ROS scavenger therapeutic potential (44, 45), probably related to their demonstrated catalytic

activity (46). In our study, we examined the effect of Au₈-pXs treatment on bone marrow-derived mesenchymal stem cells (BMSCs) from FRDA patients and found that Au₈-pXs not only acts as an antioxidant to relieve the oxidative stress improving the mitochondrial function, but also rescue the autophagy flux and increases FXN protein levels, which would be the fundamental resolution for FRDA patients. Moreover, the intravenous delivery of Au₈-pXs into YG8sR mice with advanced disease rescued many aspects of the FRDA phenotype including neuromotor and cardiac deficits, and mitochondrial response to oxidative stress. Treatment with Au₈-pXs may represent a new strategy for FRDA treatment.

Results

ROS buffering effect of Au₈-pXs.

Luminescent superstructures based on quantum metal clusters have been recently studied for their peculiar emission properties, which, coupled with an extremely high biocompatibility, pushed their evaluation as optical probes for imaging (47). Moreover, considering noble metal clusters, preliminary assays indicated a remarkable anti-cytotoxic activity of these materials (45). We recently demonstrated that in the case of Au₈ gold clusters superstructures (Au₈-pXs), this effect was correlated to a ROS-scavenging ability of the material (44), which could be linked to the reported catalytic effect of Au nanostructures on chemical and photochemical reactions involving oxygen (46, 48). We therefore investigated the possible ROS-specific interactions of Au₈-pXs aiming at pointing out a preferential pathway for their therapeutic effect on FRDA. Figure 1A shows a sketch of the molecular structure of the Au₈-pXs employed in this study, together with their UV/Vis absorption and photoluminescence profile in aqueous dispersion, respectively peaked at 380 nm and 520 nm. The superstructures have been synthesized according to the reported route as detailed in the Methods section (44). We investigated the interaction of Au₈-pXs with singlet oxygen (¹O₂^{*}), superoxide (O₂⁻) and hydrogen peroxide (H₂O₂) by

titration experiments in solution using ROS-specific sensitization methods, which enable a controlled production of the species considered in the water dispersion. The relative concentration of ROS was monitored by means of *cw* optical probing techniques. In the case of singlet oxygen, we employed as probe the fluorescent compound SOSGTM, whose photoluminescence intensity is proportional to the amount of singlet oxygen in the environment (49). Figure 1B shows the variation of the singlet oxygen amount as a function of time measured in unsealed quartz cuvettes. In the reference SOSGTM dispersion, the slight increment of +25% mirrors the spontaneous formation of singlet oxygen in the aqueous environment. By adding Au₈-pXs, none variation was observed, thus suggesting the occurrence of an interaction that reduces the final concentration of the ROS in the system. This speculation is confirmed by the experiment where the singlet oxygen amount is artificially increased by exploiting the conjugated dye Rose Bengal as photosensitizer (50). Under controlled laser excitation of Rose Bengal molecules at 473 nm, in absence of Au₈-pXs the singlet oxygen concentration increases up to +300% in the time span considered, i.e. more than one order of magnitude than the value in the reference sample. Remarkably, in presence Au₈-pXs the singlet oxygen concentration was instead progressively reduced to the level of a photosensitizer-free sample, and further decreased to reach a final value of +12%, i.e. lower than in the reference sample. By considering the mismatch between the energies of Au₈-pXs absorption, the excitation wavelength employed to activate the Rose Bengal and its emission, we avoided the inefficient photosensitization due to parasitic laser absorption by Au₈-pXs or to non-radiative energy transfer processes from Rose Bengal to Au₈-pXs, which would limit the singlet oxygen production. This way, we demonstrated an effective scavenging of the toxic species after creations in the aqueous environment.

Similar results were observed for the superoxide species. In this case, the ROS is generated by exploiting the photolysis of H₂O₂ under *cw* UV excitation at 405 nm in the aqueous solution (51), while the superoxide amount has been monitored by means of the molecular optical probe MitoSOXTM red

excited at 532 nm. As showed in Figure 1C, in absence of gold cluster superstructures, the progressive addition and photolysis of H_2O_2 rises the superoxide concentration until a saturation plateau that correspond to an increment of the ROS relative concentration of +450%. Conversely, in the same experiment performed in presence of $\text{Au}_8\text{-pXs}$, only a negligible variation of as large as +20% is observed, thus demonstrating again an excellent scavenging of superoxide.

A less effective, but still appreciable effect of $\text{Au}_8\text{-pXs}$ was observed also for the H_2O_2 species itself. The plot in Figure 1D shows the relative concentration of H_2O_2 monitored employing the diphenyl-1-pyrenylphosphine (DPPP) as molecular optical probe (52) upon progressive addition of H_2O_2 to a water solution. Despite the scavenging was not as large as in the previous cases, the reduction of the final H_2O_2 amount in presence of $\text{Au}_8\text{-pXs}$ by a factor 20% was clearly detectable. The obtained results indicate that $\text{Au}_8\text{-pXs}$, in agreement with their intrinsic chemical inertness, can interact with all the principal ROS species. Given the completely different chemical properties of the ROS considered, this result is not surprising in principle. Moreover, this apparent non-specificity agrees with the literature, where Au_n gold clusters are expected to be excellent catalyst (53) and not sacrificial agents, for different chemical and photochemical reactions (48). We then demonstrated the $\text{Au}_8\text{-pXs}$ catalytic activity for ROS degradation by means of cyclic voltammetry experiments. Figures 1E and F report the cyclic-voltammogram of a $\text{PBS}:\text{H}_2\text{O}_2$ solution in presence and absence of $\text{Au}_8\text{-pXs}$, respectively. We chose PBS as electrolyte in order to mimic the cellular electrochemical environment. The observed low reactivity with H_2O_2 allows to accurately monitor any evolution of the circulating current due to the redox reactions involving the chemical species dispersed. Figure 1E reports the cyclic voltammetry of PBS on Au electrode, in the potential range between -0.5 V and 1.0 V vs SCE. In this range PBS was completely unaffected by the applied voltage and only small capacitive current was observed. When H_2O_2 was added, a Faradaic current appears related to the redox processes of the oxygen peroxides. The oxidation peak intensity

decreased with the number of cycles, in agreement with the progressive transformation of all the H₂O₂ in solution. This signal marks the oxidation of the H₂O₂ that evolve in the production of water and oxygen molecules (54). The dynamic of the H₂O₂ oxidation was then verified in presence of Au₈-pXs. As showed, in Fig. 1F, the PBS:Au₈-pXs mixture was again electrochemically inactive at any applied voltage, thus confirming the excellent chemical stability of the gold superstructures. The cyclic voltammogram in presence of H₂O₂ was significantly different from the previous case. No current variation was detectable in correspondence of H₂O₂ oxidation potential, thus demonstrating the huge catalytic effect of the gold clusters superstructures for the oxidation reaction that immediately deplete the liquid environment from the ROS species hindering its electrochemical signature. These findings were crucial for the evaluation of Au₈-pXs as therapeutic agents. A non-sacrificial behavior means indeed that the anti-cytotoxic effect can be exploited for prolonged time until they are expelled from the biological system (*vide infra*), a process that cannot be extremely fast because of the small size << 10 nm, thus further supporting their evaluation as systemic drugs in animal models for FRDA treatment.

Au₈-pXs dependent modulation of the autophagy pathway increases mFXN levels.

Fra-taxin downregulation as in FRDA causes ROS overload, iron-sulfur (Fe-S) cluster proteins impairment and iron accumulation (17, 55, 56) leading to defects in the stability, integrity and homeostasis of mitochondria (19, 57-60). Considering our previous findings *in vitro* pointing out the ROS scavenger ability of Au₈-pXs in menadione-stressed cell lines (44), we sought to document this therapeutic potential in mesenchymal stem cells isolated from two healthy donors (BMSCs^{CTR1}, BMSCs^{CTR2}) and two age-matched FRDA patients (BMSCs^{FRDA#1}, BMSCs^{FRDA#2}). BMSCs expanded *in vitro* for three to five passages expressed high levels of CD90 (90.7%), CD73 (91.6%), CD105 (92.9%), and CD44 (91.3%) (Supplementary Figure 1). They did not display expression of hematopoietic surface

antigens CD34 and CD45, thereby confirming the mesenchymal immunophenotype (61) (Supplementary Figure 1). The optimal concentration and loading time of Au8-pXs for BMSCs treatment was determined to be within the range of 5 to 10 μ M for 24 hours, in line with our previous results (44) (Figure 2). Confocal images of BMSCs confirmed the uptake of clusters, detectable by their own fluorescence emission at 405nm laser excitation (Figure 2A and B). Thanks to their reduced dimensions, and whilst lacking targeting features, Au8-pXs partially enter mitochondria, as monitored by Mitotracker staining, indicating a widespread distribution of these clusters within different cell compartments (Figure 2B).

Considering that FXN influences several distinct mitochondrial pathways (62), we next examined the pathophysiological consequences of frataxin deficiency in iron sulfur (Fe-S) cluster biogenesis and mitochondrial metabolism of BMSCs^{FRDA}. FXN functions as an allosteric activator of the sulfur donor enzyme NFS1 and as a modulator of iron entrance into the multiprotein Fe-S cluster assembling system (63-65). This latter in presence of low FXN is unable to work at proper rate, resulting into decreased iron sulfur cluster biogenesis and activity of respiratory chain complexes, especially I, II and III (65). Overexpression of NFS1 was found in both BMSCs^{FRDA#1} and BMSCs^{FRDA#2} cells (Figure 2C and D), and the levels of NFS1 were comparable after Au8-pXs treatment (Figure 2C and D). Beyond the biochemical aspects of iron loading, mitochondrial homeostasis is also further hampered by FXN deficiency, with a dysregulation of dynamic processes such as biogenesis, fusion/fission, mitophagy and apoptosis (66, 67). In keeping with this, BMSCs^{FRDA#1} and BMSCs^{FRDA#2} cells showed increased expression of mitofusin 1 (Mfn1) compared to the BMSCs^{CTR1} and BMSCs^{CTR2} cells (P=0.0002 and P=0.0035 for BMSCs^{FRDA#1} and BMSCs^{FRDA#2}, respectively), suggesting prevalence of mitochondrial fusion over fission (68) (Figure 2C and D). These findings are in agreement with previous reports that correlated a giant morphology to a dysfunctional mitochondrion in FRDA cell and animal models (18-20, 22, 69, 70). We found that Au8-pX administration was able to determine a significant decrease of

Mfn1 expression (Figure 2C and D) with no modifications of dynamin-related protein 1 (Drp1) for both BMSCs^{FRDA#1} and BMSCs^{FRDA#2}.

The reduced levels of Mfn1 of treated BMSCs^{FRDA#1} and BMSCs^{FRDA#2} may help to isolate segments of damaged mitochondria, promoting their clearance by macroautophagy (71). As lipidation of LC3 and its association with autophagosome membranes has been established as useful sign for autophagy, we detected LC3 by immunoblotting. Importantly, a significant increase in LC3-II/LC3-I ratio was detected in both BMSCs^{FRDA#1} (P=0.0004) and BMSCs^{FRDA#2} (P=0.0016) compared to BMSCs^{CTR1} and BMSCs^{CTR2} (Figure 2C and D). On the other hand, the LC3II/LC3I ratio of Au₈-pX-treated BMSCs^{FRDA#1} and BMSCs^{FRDA#2} cells was significantly lower than their base line conditions, at both 5 and 10 μM Au₈-pX dose (Figure 2C and D). Additionally, we found increased expression of Atg7, which is required for activation of LC3II and other ubiquitin-like substrates in the autophagy pathway (72), in Au₈-pX-treated and untreated BMSCs^{FRDA#1} and BMSCs^{FRDA#2} compared to the BMSCs^{CTR1} and BMSCs^{CTR2} (Figure 2C and D). Although these positive results clearly indicate increased number of autophagosomes, nevertheless they do not always result in upregulation of the autophagic flux (73). Therefore, we measured protein levels of p62, a selective substrate of autophagy, as the activation of the autophagic flux leads to a decline in p62 expression, and vice versa (74, 75). As shown in Figure 2, a significant increase in p62 was detected in both BMSCs^{FRDA#1} and BMSCs^{FRDA#2} in comparison with respective BMSCs^{CTR}, indicating impairment in the autophagic flux. Furthermore, p62 was significantly decreased in both Au₈-pX-treated BMSCs^{FRDA#1} and BMSCs^{FRDA#2} cells, indicating a recovery of the autophagic flux. During unbalanced redox homeostasis, the p62 increases the availability and function of Nrf2 - a master regulator of antioxidant enzyme expression like glutathione peroxidase (GPx-1) (76-78). A remarkable Au₈-pX concentration-dependent increase of Nrf2 was observed in BMSCs^{FRDA#1} (Figure 2C and D). Notably, Nrf2 was less expressed in untreated BMSCs^{FRDA#1} and BMSCs^{FRDA#2} cells

(Figure 2C and D). Hence, we asked whether the recovery of the autophagic flux and Nrf2 may increase protein levels of frataxin (FXN). The FXN transcript is translated into a cytosolic precursor protein (pFXN) that is rapidly imported into mitochondria, where it is further processed from an intermediate form (iFXN) to a mature protein (mFXN), resident in the mitochondrial matrix (79). Very strikingly, we found that Au₈-pX treatment increased in a dose dependent manner the expression of total FXN in BMSCs^{FRDA#1} and BMSCs^{FRDA#2} cells (Figure 2C and D). Relatively, mFXN expression was much more robust in BMSCs^{FRDA#1} cells and the response to Au₈-pX treatment was stronger in these cells than in BMSCs^{FRDA#2} cells, where we also noted an unexpected increase of iFXN expression (Figure 2C and D). Overall, these results suggest Au₈-pX treatment determines a recovery of the mitochondria fusion leading to a rescued autophagic flux with consequent increase in FXN protein.

Recovery of the mitochondrial bioenergetic function in FRDA patient's cells treated with Au₈-pXs.

BMSCs undergo extensive metabolic changes during proliferation and differentiation processes, notably dependent on mitochondria quality and energetic processes. As the bone marrow environment is also dramatically affected by iron overload and ROS that harm the mitochondrial morphology and function during the proliferation of BMSCs (80, 81), they likely represent a model of cells highly sensitive to FXN deficiency. MTT assays indicated that the viability of BMSCs^{FRDA#1} was decreased compared to both BMSCs^{CTR} and BMSCs^{FRDA#2} (Supplementary Figure 1B) (24 hours: P=0.0002 and P<0.0001; 48 hours and 72 hours: P<0.0001 and P< 0.0001, respectively). To a lesser degree, BMSCs^{FRDA#2} displayed a slow growth becoming significant related to CTR at 72 hours (P=0.0001, Supplementary Figure 1B). These findings suggested that FXN deficiency somehow impairs BMSCs^{FRDA#1} proliferation possibly by reducing metabolic activity. We thus chose to use BMSCs^{FRDA#1},

as the line most representative for cell vulnerability in FRDA, for further metabolic studies. Interestingly, BMSCs^{FRDA#1} largely benefited from Au₈-pX uptake and, at both doses, cells grew faster than untreated cells starting from 12 hours of IncuCyte® living-cell analysis (12 hours: P<0.0001 for BMSCs^{FRDA#1} 5μM Au₈-pXs and P=0.0009 for BMSCs^{FRDA#1} 10μM; from 18 hours up to 48 hours P<0.0001 for both Au₈-pX treatments)(Figure 3A). Considering the diverse cellular adaptation depending on cluster molarity, we next assessed the *in vitro* released of ROS from BMSCs^{FRDA#1} treated with 5μM and 10 μM of Au₈-pXs for 24 hours. In line with proliferation results, we observed significantly higher levels of ROS in untreated BMSCs^{FRDA} compare to BMSCs^{CTR} (P<0.0001), which was rescued by treatment with Au₈-pX administration at both molarity (P<0.0001) (Figure 3B). Again, we detected a more effective ROS scavenger activity of 5μM Au₈-pXs (P=0.0095) compared to 10μM condition, for whose BMSCs^{FRDA#1} apparently have a less immediate response (Figure 3B). For ROS evaluation, we measured the amount of H₂O₂ that, beyond reflecting the general redox state of cells, is the reactive oxygen species with the longest half-life and easiest to detect *in vitro* (82). However, it is important to highlight that there are other ROS, including superoxide, hydroxyl radical, singlet oxygen, that can be enzymatically converted to H₂O₂ (83). Among enzymes involved in antioxidant defenses, superoxide dismutases SOD1 and SOD2 possess a preeminent role in scavenging the O₂ radicals, especially mitochondrial SOD2 converting superoxide to H₂O₂ that diffuses freely across mitochondrial membrane (84-86).

As a primary or secondary consequence of frataxin deficiency, hampered SOD signaling has been shown in FRDA patients as well as in ataxic animal models (87, 88), accompanied by inefficient response to oxidative stress and a dysfunctional mitochondrial electron transport chain. In keeping with this and the previous results showing the highly preferential buffering activity of Au₈-pXs towards oxygen singlets and superoxide species, we sought for potential effects of these clusters on mitochondrial metabolism and respiration. First, we used Seahorse Oxygen flow for the assessment of electron transport

chain (ECT) functions. We found that BMSCs^{FRDA#1} had reduced basal and maximal respiratory capacity compared to BMSCs^{CTR} (P=0.0289 and P=0.0031, respectively) (Supplementary Figure 1C). Next, we investigated bioenergetics of BMSCs^{FRDA#1} treated with 5 μ M and 10 μ M of Au₈-pXs for 24 hours (Figure 3C). Oxygen consumption rate (OCR) and extracellular acidification rate (ECAR) profiles showed an overall increase in Au₈-pXs treated BMSCs^{FRDA#1}, independently from the dose, which was most evident as basal and uncoupled (maximal) respiration (basal respiration: P=0.0471 for 5 μ M Au₈-pXs, P=0.0105 10 μ M Au₈-pXs; maximal respiration: P<0.0001 for 5 μ M Au₈-pXs, P=0.02 for 10 μ M Au₈-pXs) (Figure 3C and D). Extracellular acidification rate (ECAR, a measure of glycolysis) was also increased (Figure 3C). In addition, Au₈-pXs administration sustained an enhanced oligomycin inhibited respiration, which reflects the capacity for ATP production compared to BMSCs^{FRDA#1}. This was significant using 10 μ M Au₈-pXs condition (P=0.0363 compared to untreated BMSCs^{FRDA#1}), whereas the 5 μ M treatment showed only a trend.

Finally, we measured the mitochondrial membrane potential (MMP) as an indicator of mitochondrial integrity. MMP was detected with the lipophilic dye JC-1 by measuring a potential-dependent shift in fluorescence from green to red, which reflected its aggregation in mitochondria (89) (Figure 3E). The increased ratio of red versus green fluorescence in BMSCs^{FRDA#1} cells after Au₈-pX treatment indicated more polarized mitochondria (Figure 3E). All these data indicate that Au₈-pX treatment rescue the bioenergetic function of BMSCs^{FRDA#1} cells.

Au₈-pX engraftment in nervous and skeletal muscle systems of treated YG8sR mice

To examine whether Au₈-pXs were able to exert the ROS scavenging activity, and to trigger detoxifying pathways in a whole organism, we performed a single intravenous injection of Au₈-pXs into YG8sR murine model of FRDA. YG8sR mice (n=10) were treated when they exhibited a substantial

motor behaviour decline (12 months of age) (33, 90) and tested for 6 months after injection (18 months of age). The Au₈-pX dose was calculated considering the results obtained *in vitro* using 10 μM, which corresponds to 70g/kg (2.45 μg of Au₈-pXs per 10,000 cells that have a total weight of 35 μg). Animals of 20g weight were injected with single dose of 1.4 g of Au₈-pXs. No signs of adverse reactions such as loss of body weight, cardiac or respiratory difficulties, or skin lesions were detected in treated mice, ruling out overt *in vivo* Au₈-pXs toxicity. To verify the cluster circulation and the penetration into murine tissues, we injected YG8sR mice (n=6) with 10 μM Au₈-pXs into the tail vein. Animals were sacrificed after 30 days (n=3) or 180 days (n=3) and the gold content was evaluated by an inductively coupled plasma mass spectrometry (ICP-MS) (Supplementary Figure 2A). A group of n=6 untreated YG8sR mice was used for comparative analyses at the same time points. At 30 and 180 days, heart, brain cortex and cerebellum, basal ganglia (BGs), muscles, i.e. *quadriceps* (QAs), *tibialis anterior* (TAs), and *soleus* (SL), liver, lung, kidney and pancreas were harvested for gold element content quantification (Supplementary Figure 2A). Taking into account all the tissues, we found that Au₈-pX distribution pattern was not dependent on time, except for the liver where gold cluster superstructures highly accumulated within the first 30 days and underwent a slow hepatic clearance through time (91) (P=0.0017, compared to 180 days)(Supplementary Figure 2A). This finding suggested the long-term retention of Au₈-pX within injected tissues that may be beneficial for single infusion-based treatments. Au₈-pXs preferentially entered QAs, cerebellum, liver, cortex and TAs (Supplementary Figure 2B). Interestingly, Au₈-pXs could penetrate the BBB and gain access to the brain (Supplementary Figure 2B). This result was further confirmed by *in vivo* detection of intravenously injected Au₈-pXs by using intravital time-lapse laser confocal imaging. Vessels were visualized by a systemic administration of fluorescent antibody against CD31. *In vivo* images confirmed the migration of Au₈-pXs through the brain vessel walls, demonstrating that Au₈-pXs could pass the BBB and penetrate the surrounding tissues (Supplementary Figure 2B).

Treatment with Au₈-pXs improves neuromotor, muscle and cardiac functions in aged YG8sR mice.

We then examined whether Au₈-pX administration could rescue or protect YG8sR mice from the progressive neurobehavioral and muscular deficit characterizing FRDA disease phenotype (33, 92). Exhaustion and endurance time were evaluated by treadmill fatigue test, forcing mice to run with gradually increasing speed, while neuromuscular functions were assessed by forelimb grip strength test (Figure 4A). Functional measurements were performed in a blind to treatment assignment. Treadmill test results were expressed as total numbers of shocks received. We found that YG8sR mice were not able to sustain the exercise as demonstrated by the increased number of shocks, especially at medium and high speed test and over time (Figure 4B). Au₈-pX-treated YG8sR mice were instead less prone to fatigue and displayed better treadmill performances, independently from the work intensity (Figure 4B). The number of shocks greatly reduced in Au₈-pX treated YG8sR mice at 180 days for all the running speeds (P<0.0001 compared to YG8sR for low, medium and high intensity) (Figure 4B), with improvements observed 60 days after Au₈-pX injection for medium and high intensity exercise (60 days: P= 0.0163, medium; P=0.0007, high. 90 days: P= 0.0258, medium; P=0.0054, high. 120 days: P= 0.0002, medium; P<0.0001, high) (Figure 4B).

To gather further insights into neuromuscular functions, we performed forelimb grip strength test aiming at evaluating muscle properties, contractility and strength, at 60 and 180 days after Au₈-pX injection (Figure 4C). At 180 days, we found a general forelimb muscle weakness (Figure 4C). However, maximal strengths did not change significantly between Au₈-pXs-treated and untreated mice, suggesting that Au₈-pXs effects might be more effective in improving endurance than strength (Figure 4C).

Enhanced fatigue resistance likely results from improved cardiac functions (93). To this end, we performed echocardiographic analyses in 18 months-old untreated and Au₈-pXs-treated YG8sR mice (Figure 4D and E). The investigator performing the cardiac measurements was blinded to the identity of the treatment group. Transthoracic echocardiatic image outcomes revealed enhanced heart contractile functions in Au₈-pXs-treated YG8sR mice, as demonstrated by increased left ventricular ejection fraction (EF) (P=0.0006) and fractional shortening (FS) (P=0.0352) compared to YG8sR mice (Figure 4D). Other measurements, such as cardiac chamber dimensions and functions (Figure 4E and Table S2), suggested no major myocardial remodelling (Figure 4E). However, cardiac index ratios confirmed again a left ventricular (LV) better performance of Au₈-pXs-treated YG8sR mice. At a lesser extent, parameters describing the aortic valve (AV) functionality, such as peak pressure gradient and area, suggested more physiological hemodynamic conditions in Au₈-pX-treated compared to untreated YG8sR mice.

As observed in BMSCs^{FRDA#1} and BMSCs^{FRDA#2} cells, the QAs and hearts of Au₈-pX-treated YG8sR mice showed reduced LC3II/LC3I ratio as well as increased p62 and decreased Atg7 protein expression compared with untreated group (Figure 4F and Supplementary Figure 3). Moreover, the Au₈-pX treatment did not affected the NFS1 and Nrf2 levels in QAs and hearts of YG8sR mice (Figure 4F and Supplementary Figure 3), in parallel to a decreased amount of PGC-1 α and PPAR- γ proteins compared with untreated YG8sR mice (Figure 4F and Supplementary Figure 3). Importantly, these effects were coincident with increases in mFXN of QAs and hearts of Au₈-pX-treated YG8sR mice (Figure 4F and Supplementary Figure 3).

Subsequently, we investigated whether Au₈-pX treatment modulates the activity of the peroxisome proliferator activated receptor gamma (PPAR- γ) coactivator 1 α (PGC-1 α) as critical regulators that links metabolic activity to relevant environmental stimuli in multiple pathways affected in FRDA (94-97). Indeed, a statistically significant decrease of PPAR- γ protein levels was observed in

in QAs and hearts of Au₈-pX-treated YG8sR mice (Figure 4F and Supplementary Figure 3). Importantly, PGC-1 α level was significantly increase in QAs of Au₈-pX-treated YG8sR mice (Figure 4F and Supplementary Figure 3). Despite skeletal muscle fibrosis is not considered an overt hallmark of YG8sR, in line with the mild and variable myopathic features of FRDA patients' muscles, morphometric analysis of QAs from Au₈-pXs-treated YG8sR mice showed decreased levels of collagen deposition compared to untreated mice (0.522% \pm 0.192 vs. 2.256% \pm 0.999; P<0.0001) (Figure 4G) (31). Moreover, QA myofibers displayed a markedly smaller cross-sectional areas (CSAs) in the untreated YG8sR mice compared to those that received Au₈-pXs (YG8sR CSA mean: 605.85 \pm SD: 249.297 μ m², n=1314; Au₈-pXs treated YG8sR CSA mean: 1554.295 \pm SD:618.893 μ m², n=1314) (P<0.0001, Figure 4G), indicating an unforeseen mechanism of myofiber atrophy rescue mediated by the Au₈-pX presence. Pathophysiological signs of cardiac fibrosis and hypertrophy have been also shown to be positively affected by Au₈-pX injection (Figure 4G). Azan Mallory staining of hearts showed only a mild accumulation of collagen and perivascular fibrosis in 18 months-old Au₈-pX-treated YG8sR mice, whereas aged YG8R mice revealed disorganized cardiomyocytes, and prominent interstitial and perivascular myocardial fibrosis (0.214% \pm 0.091 vs. 3.323% \pm 0.412; P<0.0001) (Figure 4G). Fibrogenic markers as collagen VI, MMP9 and TRAF6 were significantly elevated in hearts of YG8R mice compared with Au₈-pX-treated YG8sR mice (Figure 4H and Supplementary Figure 3). Likewise, these fibrotic players were elevated in untreated QAs of YG8R mice (Figure 4H and Supplementary Figure 3). The reduction of cardiac fibrosis is in line with the high left ventricular mass and volume ratio between Au₈-pX-treated and untreated YG8R mice, which support the general improvement in both diastolic and systolic, function, and heart contractile properties of Au₈-pX-treated YG8sR mice (Figure 4H and Supplementary Figure 3).

Next, we explored whether increased muscle tone and resistance to fatigue underlined the maintenance of a functional mitochondrial network, whose content and shape contribute to muscle mass, homeostasis and metabolism (98-100). Electron microscopy images of YG8sR muscle showed a fusion network of swollen mitochondria with tubular morphology and increased number of large organelles (Figure 4I). Conversely, mitochondria in Au8-pXs-treated QA muscles exhibited small and rounded mitochondria with regular invagination of the inner membrane implying that the dysfunctional morphology of YG8sR mitochondria was restored (Figures 4I). We sought to test whether Au8-pXs treatment could alleviate FRDA pathology, with a particularly keen interest in ataxia. Balance and motor coordination impairments, occurring largely in YG8sR mouse, were evaluated by foot print test and rotarod (Figure 5A-C). The investigators performing these analyses were blinded to the identity of the treatment group. Motor coordination and locomotor activity in Au8-pX-treated and untreated YG8sR mice were assessed at 60, 120, and 180 days post injection (Figure 5A). At 180 days, Au8-pXs determined a rescue of gait alterations ($P < 0.0001$ for stride length and $P = 0.0373$ for stride width), highlighted by the footprint pattern ascribable to a high balance and coordination (Figure 5B). Consistent with the amelioration in gait analysis, balance improvement was found in Au8-pXs treated YG8sR mice 180 days after injection, when rotarod test outcomes confirmed a significantly higher latency to fall compared to untreated mice ($P = 0.0158$, Figure 5C). As both gait coordination and rotarod test give hints for determining a cerebellum dependent coordination of motor movements (101), we complemented these neuro-functional studies with western blot and immunofluorescence analysis with a focus on cerebellar tissue. To determine if the autophagy pathway is activated in degenerating Purkinje cells in YG8sR mice, we performed LC3/p62/Atg7 western blot analysis on cerebellar lysates from 18 months-old untreated and Au8-pXs treated YG8sR mice (Figure 5D). The cerebellum of Au8-pX-treated YG8sR mice showed reduced LC3II/LC3I ratio as well as increased p62 and Atg7 protein expression compared with untreated

group (Figure 5D and Supplementary Figure 4). In addition, NFS1 and Nrf2 were significantly elevated in cerebellum of Au8-pX-treated YG8sR mice in association to increased amount of PGC-1 α and PPAR- γ proteins (Figure 5D and Supplementary Figure 4). Notably, these effects were coincident with increases of mFXN in cerebellum of Au8-pX-treated YG8sR mice (Figure 5D and Supplementary Figure 4). Altogether, these results indicate a recovery of autophagic flux and restoration of some of the antioxidant signaling events, offering a potential explanation for why FXN increases in cerebellum after Au₈-pX treatment (102). Cerebellar Purkinje cells are enriched for FXN protein expression and have previously been shown to undergo notable damage in samples from FRDA patients and animal models (103, 104). We thus examined Purkinje cells with parvalbumin staining, a calcium binding protein, which regulates neuronal firing properties (105). Consistent with previous studies (17, 104), the number of parvalbumin positive Purkinje cells was reduced in YG8sR mice, whereas the number of these cells was blunted in Au8-pX-treated YG8sR mice (Figure 5E). Importantly, the Au₈-pX treatment markedly reduced neuronal loss within the cerebellar dentate nucleus with amplification of the pool of calbindin positive Purkinje cell layer (Figure 5F). Moreover, cellular glutathione peroxidase (GPx-1) was reduced and predominately localized around vessels of microglia of Au₈-pX treated mice (Figure 5F). All these histopathological findings, together with the motor-functional results, indicate that Au₈-pX treatment is capable of blunting neurological disease in YG8sR mice.

Treatment with Au₈-pXs does not affect glucose intolerance in aged YG8sR mice.

Diabetes mellitus and glucose intolerance are additional non-neurological symptoms affecting FRDA patients (106) that have been attributed to pancreas degeneration determined by senescence pathway and apoptotic processes occurring in insulin producing β -cells (107, 108). In addition, a high percentage of FRDA patients have muscle insulin resistance (109), which can be a complementary cause

of hyperglycaemia, reduced glucose uptake and poor exercise performance. As YG8sR animal models resemble patients' impaired glucose metabolism and pancreas degeneration (106), we performed fasting glucose (GTT) and insulin (ITT) tolerance to verify a role of Au₈-pXs in increasing muscle insulin sensitiveness and endurance (Supplementary Figure 5). In GTT experiments, Au₈-pXs-treated and untreated YG8sR mouse glycaemia was recorded before (as baseline) and up to one hour after 1mg/g glucose injection. Unexpectedly, baseline blood glucose concentrations from both groups kept within normal ranges (<200mg/dl) (REF) throughout 180 days of the *in vivo* experiments, indicating a condition probably preceding overt diabetes (Supplementary Figure 5A). However, glycaemic curves showed instead a trend towards elevated values after glucose injection (≥ 200 mg/dl), especially 20 and 40 minutes later, suggesting a mild glucose intolerance in the YG8sR mice (Supplementary Figure 5A). There were no significant differences in GTT parameters between Au₈-pXs-treated and untreated YG8sR mice, but at 180 days post Au₈-pXs treatment the YG8sR mice showed a modest reduction of glucose intolerance compared to untreated YG8sR mice (Supplementary Figure 5A). Subsequent ITT showed that both Au₈-pXs-treated and untreated YG8sR mice have enhanced glucose utilisation after insulin injection (0.75 U/kg), suggesting insulin hypersensitivity (Supplementary Figure 5B). Therefore, our findings are consistent with a mild glucose intolerance in YG8sR mice that do not appear to respond to the Au₈-pXs treatment.

Au₈-pXs treatment restores physiological stress and redox pathways of YG8sR mice

Encouraged by *in vitro* findings, we next sought for mitochondrial functions and changes of oxidative stress and damage parameters in Au₈-pXs treated YG8sR mouse tissues. Of note, we found an increased mRNA levels of genes coding for antioxidant proteins such as *peroxyredoxin* (*Prdx2*)($P < 0.0001$), *glutathion-S-transferase* (*Gstm1*)($P = 0.0008$) and *Nrf2* ($P = 0.0102$) in the dorsal root

ganglia (DRG) of Au₈-pXs treated YG8sR mice (Figure 6A), a tissue commonly presenting with severe injury in this tissue (110). Along with these results, there was a general but variable increase of antioxidant enzymes mRNAs in the CNS (cortex, cerebellum and BGs), suggesting priming of mobilization of defences against oxidative stress (Figure 6A). We next investigated the cumulative damaging effects of ROS, namely the lipid peroxidation and the DNA oxidative damage, in tissue samples of the CNS, skeletal muscles (TAs, QAs and SL) and hearts of Au₈-pXs injected mice (Figure 6B). Compared to control untreated samples, in total and mitochondrial extracts of the CNS and skeletal muscles from the Au₈-pXs-treated mice we detected a significant reduction of 4-Hydroxynonenal (4-HNE), a stable product of lipid peroxidation, and 8-oxo-deoxy-guanosine (8-oxodG), a stable product of ROS-dependent DNA damage (Figure 6B). YG8sR-treated hearts showed a slight decrease of both parameters, suggesting the occurrence of tissue specific abilities to mount antioxidant strategies that work at different rate and efficiency. Consistent with a reduced requirement and/or consumption of the antioxidant molecule GSH and improved detoxifying activity occurring in CNS and muscles of Au₈-pXs-treated mice, we found higher GSH level and GST activity accompanied to GSSG decrease (Figure 6C). Since Nrf2 is a transcriptional inducer of SOD, a key enzyme in preventing ROS increase (111), we measured the activity of SOD1 and SOD2 in Au₈-pXs-treated and untreated tissues (Figure 6D). While cytosolic SOD1 levels remained unchanged, we noticed an increased activity of mitochondrial SOD2 (Figure 6D). We thus focused on the effects of Au₈-pXs on mitochondria oxidative energy metabolism, and we measured the level of mitochondrial ATP and the efficiency of electron transport chain in Au₈-pXs-treated YG8sR mice (Figure 6E). In the CNS and skeletal muscle tissues examined, as well as in the heart, the efficiency of electron transport chain, using a combined complex I+III activity as surrogate, and the level of mitochondrial ATP were significantly increased in tissues of Au₈-pXs-treated animals (Figure 6E). Overall, these data showed that injection of Au₈-pXs ameliorates the pathology of frataxin

loss in YG8sR mice by reducing oxidative damage and improving mitochondrial function. This rescue was significant in CNS and muscle tissues and consistent with neuromotor and cardiac functional improvement; however, Au₈-pXs failed to determine such differences in the pancreas, and in fact glucose tolerance and insulin resistance remained similarly compromised in untreated and treated YG8R mice (Supplementary Figure 5).

Discussion

Currently, there is no effective therapy for FRDA and only limited treatment for the management of debilitating symptoms. Preclinical stem cell or gene therapies have been tested to increase the amount of FXN as the most effective therapeutic approach (39, 70, 112). Since the lack of mitochondrial FXN is the primary cause, reducing oxidative damage and alleviating mitochondrial dysfunction could be a valid alternative strategy. Clinical trials with compounds such as idebenone, MitoQ, CoQ10, and vitamin E, that exert protection from H₂O₂ oxidative damage, have had limited success suggesting that frataxin deficiency modified various mitochondrial and cellular regulatory mechanisms still not fully understood. Here we demonstrated that Au₈-pXs possess broad catalytic effects against singlet oxygen, superoxide and hydrogen peroxide. Moreover, single dose systemic injection of Au₈-pXs into aged affected YG8Rs mice ameliorates the FRDA pathology, including neurobehavioral deficits, muscle endurance and heart contractile dysfunctions. The key advantage of this treatment is the capacity of the Au₈-pXs to migrate across the vessels and BBB and remain for prolonged time in several tissues including muscles, heart and cerebellum of YG8sR mouse. Importantly, the neurological phenotypic rescue observed in Au₈-pXs-treated YG8sR mice may be, in part, due to the expansion of the pool of cerebellar Purkinje cell layer. All these histopathological and motor-functional results indicate that Au₈-pX treatment is capable of blunting the oxidative stress of YG8sR mice. Our findings showed that Au₈-pXs buffer intra-

mitochondrial ROS by increasing SOD2 activity. This buffer activity prevents the oxidative damage on total DNA and membrane, allowing a higher efficacy of ETC and synthesis of ATP. Moreover, the buffered mitochondrial ROS allows to spare GSH for detoxification reactions, as demonstrated by the increased activity of GST, enhancing the protection from endogenous or exogenous oxidative stresses in treated tissues. This condition results in lower oxidative damages in whole cell membranes and nuclear DNA that are two components only indirectly touched by the oxidative mitochondrial damage induced by mutated FXN. These results are in line with our previous data reporting the ability of Au₈-pXs to scavenge ROS (44). Thus, compared to other antioxidants treatments that specifically target mitochondria or cell membranes, the Au₈-pXs seems to act as multi-target protective agents in both FRDA cells and YG8sR mouse.

We showed that Au₈-pX treatment of FRDA cell and YG8sR animal model determines the recovery of autophagy flux. These data may support that the excessive production of ROS in FRDA models could increase cell damage, while the role of autophagy could exhibit duality. In fact, initiated autophagy by oxidative stress could clear mitochondria and proteins damaged by ROS suggesting that autophagy, in turn, may contribute to reduce levels of ROS by different pathways such as p62 delivery and mitophagy pathways. In addition, increasing evidence supports the notion that autophagy is critical for the survival or death of cells suggesting a double-edged sword (113, 114). The physiological levels of autophagy are extremely important in maintaining cellular homeostasis through continuous turnover of nonfunctional proteins and organelles, whereas insufficient or excessive levels of autophagy may promote cell death due to breaking cellular homeostasis. However, the specific molecular mechanisms of this double role remain unclear. YG8sR muscles showed a tubular pattern that indicates fusion activity of the mitochondrial network. However, we found in BMSCs^{FRDA} cells the induction of mitochondrial Mfn1 fusion protein associated with high OXPHOS activity and an increase in mitochondrial membrane

potential. This response of mitochondrial physiology may result from the mitochondrial network effort to buffer respiratory defects and oxidative stress (115, 116). Hyperfused mitochondria should protect cells from apoptotic cell death whereas the increased expression of the autophagy LC3II and Atg7 markers with reduced p62 in BMSCs^{FRDA} suggests that the reduction of frataxin impair autophagy flux in basal conditions. Notably, Au₈-pXs treatment of BMSCs^{FRDA} and YG8sR mouse determined the decrease of LC3II/LC3I and increase of p62 suggesting the recovery of the autophagic flux (117-119). Impaired autophagy could be critical in modulating Nrf2 degradation and activity. Therefore, Nrf2 regulates the transcription and expression of autophagy genes that actively participate in protein degradation and ROS recovery.

We observed increased expression of Nrf2 in Au₈-pXs-treated BMSCs^{FRDA#1} and in cerebellum of Au₈-pXs-treated YG8sR mouse. Activated Nrf2 binds the antioxidant-responsive element (ARE motif) located in the p62 promoter to promote the expression of p62 mRNA. P62, in turn, positively regulates the transcription of Nrf2 (120). p62 is also a substrate for lysosomal proteases. Hence, stimuli such as hypoxia and amino acid deprivation have been shown to induce autophagy, as well as p62 degradation and, subsequently, decrease p62 intracellular levels (78). BMSCs^{FRDA} showed impaired Nrf2 activation and reduced p62 levels, thus increasing oxidative stress. Surprisingly, Nrf2 increase was associated to increased expression of mFXN in Au₈-pXs-treated BMSCs^{FRDA#1} and in cerebellum of Au₈-pXs-treated YG8sR mouse. The FXN transcript is translated into a cytosolic precursor protein (pFXN) that is rapidly imported into mitochondria, where it is further processed from an intermediate form (iFXN) to a mature protein (mFXN) (79). The increased expression of mFXN should be able to potentiate the antioxidant responses of Au₈-pXs. Of note, this later effect was coincident with a significant increase of PGC-1 α and PPAR- γ protein levels in Au₈-pXs-treated cerebellum tissue. PGC-1 α and PPAR- γ have been associated to increased protein levels of FXN (16, 102). In contrast, the recovery of the autophagic

flux in Au₈-pXs-treated heart and QAs muscle tissues was not accompanied by increased Nrf2, PGC-1 α , PPAR- γ and mFXN levels. This is intriguing and contrasts with the functional ameliorations observed in cardiac and muscle tissues. One possible explanation for such a difference is the diverse regulation of autophagy-mediated signaling pathway in different cell types and tissues such as heart, muscle and cerebellum. Overall, these data indicate a mechanistic pathway of Au₈-pXs treatment based on the reduction of the oxidative damage coupled with the recovery of mitochondrial energetic metabolism and autophagy flux.

Systemic delivery of Au₈-pXs appears to have several advantages, for instance the ability to target different cell types within multiple tissues including nervous tissues. Although pancreas endocrine defects remain unchanged, we showed a significant improvement of the motor and heart function with amelioration of the FRDA hallmarks in Au₈-pXs-treated nervous, skeletal muscle and cardiac tissues of YG8sR. Our observations that Au₈-pX treatment can attenuate neurological disease in a mouse model of FRDA have important clinical implications. First, from a therapeutic perspective it predicts that Au₈-pX agents may have therapeutic potential for FRDA leading to future challenges lie in identifying strategies by which the insights from the current work can be safely and practically translated into patients. Second, and perhaps of more immediate relevance, our work predicts that autophagy may in fact be detrimental to patients with FRDA. It will be important to perform further analyses to determine whether autophagy correlates with disease progression in FRDA patients. In summary, it is reasonable to suggest that a single infusion of Au₈-pXs may represent a promising approach for non-genetic treatment of FRDA.

MATERIALS AND METHODS

Study design

The primary aim of this study was to transfer the ROS scavenger activity of catalysts gold cluster superstructures Au₈-pXs into FRDA pathology, whose degenerative phenotype is linked to oxidative stress activated signaling. In vitro, we used BMSCs derived from FRDA patients and age matched healthy donors to identify short term Au₈-pX mechanisms of action, directly attributable to ROS buffering abilities. Considering that gold clusters superstructures did not act as sacrificial agents, we established the activation of a late/secondary response to Au₈-pX injection into the YG8sR model of Fredrich's ataxia. This effect was examined in murine tissues particularly affected by frataxin deficiency, such as central, peripheral nervous system, and heart, as well as in mildly damaged skeletal muscles and pancreas. FRDA patients (n=2) and healthy donors (n=2) were enrolled for bone marrow harvesting in the Unit of Neurology of the Fondazione IRCCS Ca' Granda Ospedale Maggiore Policlinico in Milan, Italy. The study was approved by the Institutional Ethics Committee (02.04.2013, n. 792), and samples collected with informed consent in accordance with the guidelines of the Committee on the Use of Human Subjects in Research of the Policlinico Hospital of Milan. All the animal procedures were approved by the local Animal Ethics Committee of the Department of Molecular Biotechnology and Health Sciences of Turin and the Ministry of Health (PR 72833). Animals were maintained according to institutional animal welfare guidelines and legislation, and under veterinarian surveillance. The evaluation of Au₈-pX effects, in vitro and in vivo, has been performed by Western blot and immunostaining analyses. Experiments involving cell cultures were replicated independently at least three times per experiment, while experiments involving murine tissues at least twice. In vivo outcomes have been further supported by RT-PCR and biochemical analysis of Au₈-pXs mediated rescue from oxidative stress and damages associated to FRDA degeneration, as well as by skeletal and cardiac muscle

function measurements. To verify the cluster circulation and the penetration into murine tissues, 12 months-old YG8sR mice (n=6) were injected with 10 μ M Au₈-pXs into the tail vein. Age matched YG8sR mice (n=6) were used as controls. Animals were sacrificed after 30 days (n=3 per experimental group) or 180 days (n=3 per experimental group). For in vivo imaging 12 months old Au₈-pXs treated and untreated YG8sR mice (n=3 mice per group) were used. For Au₈-pX treatment, 12 months-old animals were randomly assigned to experimental groups (n=10 Au₈-pXs treated YG8sR vs. n=10 untreated YG8sR) on the day of injection. Histology score and motor behavior test were performed in a blind manner.

Statistical analysis

Statistical analyses were performed using GraphPad prism software (version 8.4). P values and statistically significant differences were determined by two-sided Student's *t* test, for comparison between two groups, or ordinary one-way ANOVA, for comparison among more than two groups. P values were corrected for multiple comparison by post hoc Bonferroni's test. P values <0.05 were considered statistically significant (as detailed in the figure legends).

Mouse strains

The YG8sR *Frataxin* mice were obtained from Jackson Laboratory (#024113). This model better recapitulates the human FDRA phenotype (33). Specifically, beginning in adult age, these mice show motor coordination deficits, cardiac dysfunctions, and histological signs of cell damage in the brain, muscles, DRG. Animals appeared overall normal, could feed and reproduce normally, with signs of ataxia beginning after 8 months of age (33). Animals were maintained in a mixed C57/BL6: DBA genetic background. Primers used for genotyping are reported in Table S1.

BMSCs^{FRDA} labeling with Au₈-pXs

In keeping with previous results [Santiago-Gonzalez, 2016 #47], we set up the optimal conditions for the loading of BMSCs^{FRDA} with Au₈-pXs. The aim was to achieve the highest compatibility with cell viability and proliferation, as well as the strongest ROS buffering activity. For this purpose, we labeled the BMSCs^{FRDA} for 24 hours with 5 or 10 μ M Au₈-pXs, by directly adding the gold cluster solution into fresh DMEM/F12 medium supplemented with 10% FBS. Cells were then washed twice in PBS, in order to remove any floating debris and Au₈-pXs that were not internalized and primed for further analyses.

Staining of mitochondria

10,000 Au₈-pXs labeled and unlabeled BMSCs from FRDA patients were stained for mitochondria into 4-well chamber slides with MitoTrackerTM Red CMXRos (Thermo Fisher Scientific). Cells were treated with 50nM MitoTrackerTM Red CMXRos in cell culture medium without serum for 30 minutes at 37°C, and then fixed with 4% paraformaldehyde (PFA) (Thermo Fisher Scientific) for 10 minutes. Leica SP8 confocal microscope was used to acquire images. Au₈-pXs fluorescence was detected setting the emission range between 500 and 540 nm under 405 nm excitation. Each cell group was evaluated in five independent experiments. Colocalization of mitochondria and gold clusters superstructures was evaluated by EZColocalization plugin of Image J, identifying single cells through hand drawn ROIs. The result was represented as heatmap image between 0 and 250.

Seahorse test and mitochondrial membrane potential analysis.

Oxygen consumption rate (OCR) was measured using a Seahorse XFp Mito Stress Test kit (Agilent). BMSCs^{FRDA#1} were plated at density 10,000 cell/ well onto 8-well XFp microplates (Agilent) and grown overnight in DMEM/F12 medium culture supplemented with 5mM D-glucose (low glucose)

(Sigma Aldrich), 2mM L-glutamine (Gibco- Thermo Fisher Scientific), 10% FBS and 0.1% gentamycin. Cells were then treated with 5 or 10 μ M Au₈-pXs for 24 hours. Not treated BMSCs^{FRDA#1} were used for comparison. For Seahorse analysis, cells were preincubated in Seahorse fresh medium supplemented only with 2mM L-glutamine at pH7.4 for 1 hour at 37°C in a non-CO₂ incubator. Mitochondrial respiration changes were measured basally and after the subsequent injections of 2.5 μ M oligomycin (Sigma Aldrich), 0.5 μ M FCCP (Sigma Aldrich) and 1 μ M Rotenone/Antimycin (R/A) (Sigma Aldrich). Before each injection 4 measurements of OCR were recorded. Data were normalized on total protein, quantified by DC protein assay (Bio-rad). Basal and maximal respiration, ATP production, proton leak, spare capacity and non-mitochondrial respiration were calculated and analyzed with the Seahorse wave Software (Agilent). Each condition was evaluated in duplicate or triplicate for three independent experiments. Mitochondrial membrane potential was measured with JC-1 dye (Abcam) according to manufacturer's instruction. Briefly, 10,000 Au₈-pXs labeled BMSCs^{FRDA#1}, BMSCs^{FRDA#1}, and BMSCs^{CTR} seeded in a black wall 96-well plate were stained at 37°C for 30 minutes with 5 μ g/ml JC-1 dye. Cells were then wash twice in warm PBS and emission of monomers and aggregates was detected through 530 \pm 15 and 585 \pm 20 nm filters with Glomax Discover plate reader. Data were represented as ratio between 590/530 fluorescence emission. Each condition was evaluated in five independent experiments.

In vivo intra-arterially injection of Au₈-pXs

YG8sR mice were treated at 12 months of age, when signs of motor behavior deficit and poor endurance and fatigue occurred. N=10 YG8sR mice were randomly chosen for injection (Au₈-pXs treated YG8sR). 1.4 g of Au₈-pXs in 100 μ l PBS were mixed thoroughly and injected into the tail vein of YG8sR mice. N=10 YG8sR mice, age matched, were considered as controls.

Motor behaviour tests

Endurance and muscle strength

Resistance to physical exercise was tested with the treadmill apparatus, essentially as described (121, 122). Briefly, mice were placed on a transparent treadmill belt (Cleverly Sys Inc), with a constant 10% slope, and with a step-wise increasing rotation speed. The following program was used: speed 18 cm/sec, from 0 to 10 minutes; speed 28 cm/sec, from 10 to 20 minutes, speed 38 cm/sec, from 20 to 25 minutes, speed 42 cm/sec, from 25 to 30 minutes, and speed 46 cm/sec, from 30 to 35 minutes. Data were recorded at 38 cm/sec (low intensity), 42 cm/sec (medium intensity), and 46 cm/sec (high intensity). At each time point the number of accumulated shocks was recorded; in case of evident physical exhaustion before the end of the test, animals are removed from the apparatus and an arbitrary value was assigned based on the total traveled distance. First signs of decreased endurance performance were clearly noticeable by treadmill around the 11th month of age in YG8sR mice (B.I.). Mice were then treated with Au₈-pXs and tested on treadmill after 20, 60, 90, 120 and 180 days from the injection. The grip strength meter (Salter Brecknell Model 12 Spring Balance) was used to assess the forelimb grip strength of Au₈-pXs treated and untreated YG8sR. The peak force was measured in four trials with a rest period of 5 minutes between each trial. Muscle strength was evaluated 60 and 180 days after Au₈-pX injection.

Balance coordination and gait analysis

Motor coordination ability was assessed using a Ugo-Basile 7650 accelerating rotarod treadmill (123). N=4 trials were performed with the speed of the rotation gradually increasing from 4 to 40 rpm and each trial lasted approximately 3 to 5 minutes, separated by a rest period of 200 sec between each trial. The latency to fall was recorded and the maximum time on the rotarod was set at 400 sec. As for treadmill, rotarod test was performed B.I., and after 20, 60, 90, 120 and 180 days from the Au₈-pX

injection. To obtain the footprints, mouse paws were dipped in nontoxic water-based food dye (124). The mice were allowed to walk along a 40-cm long, 9.5-cm wide, gangway (with 7-cm-high side walls) with white paper lining the floor. All mice had one training run and were then given three trials. For each mouse, three steps from the middle portion of each run were considered for stride length and width measurement. Foot print analysis was performed 60, 120 and 180 days after Au₈-pX injection.

Histology and immunofluorescence of murine tissues

For histology and immunofluorescence staining, tissues were collected from Au₈-PXs treated and untreated YG8sR, frozen in liquid nitrogen cooled isopentane for 30 seconds and cut in 8µm sections on cryostat (Leica Biosystems). For Azan Mallory staining of fibrosis, sections of QAs and hearts were stained, dried in increasing concentration of ethanol, clarified with xylene (Sigma Aldrich) and mounted with Vectamount (Vector Laboratories) (125). Images were captured with a Leica DM6000B optical microscope (Leica Biosystems). Percentage of fibrosis in QAs and hearts was quantified through Threshold color Plugin of ImageJ Software. QA myofiber area was quantified by manual counting of fiber number and analysed by ImageJ software as already described (125).

Immunofluorescence staining were performed on cerebellum sections. Tissue was fixed in 4% PFA for 15 minutes at room temperature, then permeabilized with 0.5% Triton X-100 (Sigma Aldrich) for 10 minutes and blocked for 1 hour with 5% normal serum (FBS, horse serum or donkey serum) with 0.1% Triton X-100. 0.1M glycine incubation for 15 minutes was performed to reduce background from unreacted aldehydes, when needed. Incubations with primary antibodies (dilution 1:100 in blocking solution) were performed at 4°C overnight with: anti-parvalbumin (Abcam), anti-Calbindin D (EMD, Millipore), anti NeuN (Chemicon International) and anti-Glutathione peroxidase (GPx-1) (Abcam). Appropriate Alexa Fluor conjugated secondary antibodies (Thermo Fisher Scientific) were incubated for

1hour diluted 1:200 in PBS. Staining for conjugated anti-GFAP Cy3 (Sigma Aldrich) was performed for 1 hour with 1:100 dilution in PBS, while NeuroTrace 647 (Thermo Fisher Scientific) staining was performed following manufacturer's instructions. Nuclei were counterstained with DAPI (Thermo Fisher Scientific) and sections were mounted with Fluoromount-G Mounting Medium (Thermo Fisher Scientific). Images and z-stacks reconstructions were acquired with a SP8 confocal microscope (Leica Biosystems)

References

1. V. Campuzano, L. Montermini, Y. Lutz, L. Cova, C. Hindelang, S. Jiralerspong, Y. Trottier, S. J. Kish, B. Faucheux, P. Trouillas, F. J. Authier, A. Durr, J. L. Mandel, A. Vescovi, M. Pandolfo, M. Koenig, Frataxin is reduced in Friedreich ataxia patients and is associated with mitochondrial membranes. *Human molecular genetics* **6**, 1771-1780 (1997).
2. V. Campuzano, L. Montermini, M. D. Molto, L. Pianese, M. Cossee, F. Cavalcanti, E. Monros, F. Rodius, F. Duclos, A. Monticelli, F. Zara, J. Canizares, H. Koutnikova, S. I. Bidichandani, C. Gellera, A. Brice, P. Trouillas, G. De Michele, A. Filla, R. De Frutos, F. Palau, P. I. Patel, S. Di Donato, J. L. Mandel, S. Coccozza, M. Koenig, M. Pandolfo, Friedreich's ataxia: autosomal recessive disease caused by an intronic GAA triplet repeat expansion. *Science* **271**, 1423-1427 (1996).
3. M. Pandolfo, Iron metabolism and mitochondrial abnormalities in Friedreich ataxia. *Blood cells, molecules & diseases* **29**, 536-547; discussion 548-552 (2002).
4. J. Gerber, U. Muhlenhoff, R. Lill, An interaction between frataxin and Isu1/Nfs1 that is crucial for Fe/S cluster synthesis on Isu1. *EMBO reports* **4**, 906-911 (2003).
5. R. Lill, Function and biogenesis of iron-sulphur proteins. *Nature* **460**, 831-838 (2009).
6. M. Ristow, M. F. Pfister, A. J. Yee, M. Schubert, L. Michael, C. Y. Zhang, K. Ueki, M. D. Michael, 2nd, B. B. Lowell, C. R. Kahn, Frataxin activates mitochondrial energy conversion and oxidative phosphorylation. *Proceedings of the National Academy of Sciences of the United States of America* **97**, 12239-12243 (2000).

7. P. R. Anderson, K. Kirby, W. C. Orr, A. J. Hilliker, J. P. Phillips, Hydrogen peroxide scavenging rescues frataxin deficiency in a *Drosophila* model of Friedreich's ataxia. *Proceedings of the National Academy of Sciences of the United States of America* **105**, 611-616 (2008).
8. S. Chiang, D. S. Kalinowski, P. J. Jansson, D. R. Richardson, M. L. Huang, Mitochondrial dysfunction in the neuro-degenerative and cardio-degenerative disease, Friedreich's ataxia. *Neurochemistry international* **117**, 35-48 (2018).
9. E. Cadenas, K. J. Davies, Mitochondrial free radical generation, oxidative stress, and aging. *Free radical biology & medicine* **29**, 222-230 (2000).
10. S. Petrillo, E. Piermarini, A. Pastore, G. Vasco, T. Schirinzi, R. Carrozzo, E. Bertini, F. Piemonte, Nrf2-Inducers Counteract Neurodegeneration in Frataxin-Silenced Motor Neurons: Disclosing New Therapeutic Targets for Friedreich's Ataxia. *International journal of molecular sciences* **18**, (2017).
11. V. D'Oria, S. Petrini, L. Travaglini, C. Priori, E. Piermarini, S. Petrillo, B. Carletti, E. Bertini, F. Piemonte, Frataxin deficiency leads to reduced expression and impaired translocation of NF-E2-related factor (Nrf2) in cultured motor neurons. *International journal of molecular sciences* **14**, 7853-7865 (2013).
12. S. Sahdeo, B. D. Scott, M. Z. McMackin, M. Jasoliya, B. Brown, H. Wulff, S. L. Perlman, M. A. Pook, G. A. Cortopassi, Dyclonine rescues frataxin deficiency in animal models and buccal cells of patients with Friedreich's ataxia. *Human molecular genetics* **23**, 6848-6862 (2014).
13. A. Anzovino, S. Chiang, B. E. Brown, C. L. Hawkins, D. R. Richardson, M. L. Huang, Molecular Alterations in a Mouse Cardiac Model of Friedreich Ataxia: An Impaired Nrf2 Response Mediated via Upregulation of Keap1 and Activation of the Gsk3beta Axis. *The American journal of pathology* **187**, 2858-2875 (2017).

14. A. Kobayashi, M. I. Kang, H. Okawa, M. Ohtsuji, Y. Zenke, T. Chiba, K. Igarashi, M. Yamamoto, Oxidative stress sensor Keap1 functions as an adaptor for Cul3-based E3 ligase to regulate proteasomal degradation of Nrf2. *Molecular and cellular biology* **24**, 7130-7139 (2004).
15. M. J. Jasoliya, M. Z. McMackin, C. K. Henderson, S. L. Perlman, G. A. Cortopassi, Frataxin deficiency impairs mitochondrial biogenesis in cells, mice and humans. *Human molecular genetics* **26**, 2627-2633 (2017).
16. D. Marmolino, M. Manto, F. Acquaviva, P. Vergara, A. Ravella, A. Monticelli, M. Pandolfo, PGC-1alpha down-regulation affects the antioxidant response in Friedreich's ataxia. *PloS one* **5**, e10025 (2010).
17. H. Lin, J. Magrane, A. Rattelle, A. Stepanova, A. Galkin, E. M. Clark, Y. N. Dong, S. M. Halawani, D. R. Lynch, Early cerebellar deficits in mitochondrial biogenesis and respiratory chain complexes in the KIKO mouse model of Friedreich ataxia. *Disease models & mechanisms* **10**, 1343-1352 (2017).
18. H. Puccio, D. Simon, M. Cossee, P. Criqui-Filipe, F. Tiziano, J. Melki, C. Hindelang, R. Matyas, P. Rustin, M. Koenig, Mouse models for Friedreich ataxia exhibit cardiomyopathy, sensory nerve defect and Fe-S enzyme deficiency followed by intramitochondrial iron deposits. *Nature genetics* **27**, 181-186 (2001).
19. N. Calmels, H. Seznec, P. Villa, L. Reutenauer, M. Hibert, J. Haiech, P. Rustin, M. Koenig, H. Puccio, Limitations in a frataxin knockdown cell model for Friedreich ataxia in a high-throughput drug screen. *BMC neurology* **9**, (2009).
20. A. Hick, M. Wattenhofer-Donze, S. Chintawar, P. Tropel, J. P. Simard, N. Vaucamps, D. Gall, L. Lambot, C. Andre, L. Reutenauer, M. Rai, M. Teletin, N. Messaddeq, S. N. Schiffmann, S. Viville, C. E. Pearson, M. Pandolfo, H. Puccio, Neurons and cardiomyocytes derived from induced

pluripotent stem cells as a model for mitochondrial defects in Friedreich's ataxia. *Disease models & mechanisms* **6**, 608-621 (2013).

21. A. Bolinches-Amoros, B. Molla, D. Pla-Martin, F. Palau, P. Gonzalez-Cabo, Mitochondrial dysfunction induced by frataxin deficiency is associated with cellular senescence and abnormal calcium metabolism. *Frontiers in cellular neuroscience* **8**, 124 (2014).
22. E. Obis, V. Irazusta, D. Sanchis, J. Ros, J. Tamarit, Frataxin deficiency in neonatal rat ventricular myocytes targets mitochondria and lipid metabolism. *Free radical biology & medicine* **73**, 21-33 (2014).
23. M. J. Czaja, Functions of autophagy in hepatic and pancreatic physiology and disease. *Gastroenterology* **140**, 1895-1908 (2011).
24. N. Mizushima, Physiological functions of autophagy. *Current topics in microbiology and immunology* **335**, 71-84 (2009).
25. Y. Ichimura, T. Kirisako, T. Takao, Y. Satomi, Y. Shimonishi, N. Ishihara, N. Mizushima, I. Tanida, E. Kominami, M. Ohsumi, T. Noda, Y. Ohsumi, A ubiquitin-like system mediates protein lipidation. *Nature* **408**, 488-492 (2000).
26. M. Komatsu, Y. Ichimura, Physiological significance of selective degradation of p62 by autophagy. *FEBS letters* **584**, 1374-1378 (2010).
27. P. H. Reddy, Misfolded proteins, mitochondrial dysfunction, and neurodegenerative diseases. *Biochimica et biophysica acta* **1842**, 1167 (2014).
28. P. H. Reddy, Increased mitochondrial fission and neuronal dysfunction in Huntington's disease: implications for molecular inhibitors of excessive mitochondrial fission. *Drug discovery today* **19**, 951-955 (2014).
29. M. Pandolfo, Friedreich ataxia: the clinical picture. *Journal of neurology* **256 Suppl 1**, 3-8 (2009).

30. S. Chiang, Z. Kovacevic, S. Sahni, D. J. Lane, A. M. Merlot, D. S. Kalinowski, M. L. Huang, D. R. Richardson, Frataxin and the molecular mechanism of mitochondrial iron-loading in Friedreich's ataxia. *Clinical science* **130**, 853-870 (2016).
31. A. H. Koeppen, J. E. Mazurkiewicz, Friedreich ataxia: neuropathology revised. *Journal of neuropathology and experimental neurology* **72**, 78-90 (2013).
32. B. Carletti, F. Piemonte, Friedreich's Ataxia: A Neuronal Point of View on the Oxidative Stress Hypothesis. *Antioxidants* **3**, 592-603 (2014).
33. S. Anjomani Virmouni, V. Ezzatizadeh, C. Sandi, M. Sandi, S. Al-Mahdawi, Y. Chutake, M. A. Pook, A novel GAA-repeat-expansion-based mouse model of Friedreich's ataxia. *Disease models & mechanisms* **8**, 225-235 (2015).
34. D. R. Richardson, Friedreich's ataxia: iron chelators that target the mitochondrion as a therapeutic strategy? *Expert opinion on investigational drugs* **12**, 235-245 (2003).
35. M. L. Jauslin, T. Meier, R. A. Smith, M. P. Murphy, Mitochondria-targeted antioxidants protect Friedreich Ataxia fibroblasts from endogenous oxidative stress more effectively than untargeted antioxidants. *FASEB journal : official publication of the Federation of American Societies for Experimental Biology* **17**, 1972-1974 (2003).
36. R. Lodi, P. E. Hart, B. Rajagopalan, D. J. Taylor, J. G. Crilley, J. L. Bradley, A. M. Blamire, D. Manners, P. Styles, A. H. Schapira, J. M. Cooper, Antioxidant treatment improves in vivo cardiac and skeletal muscle bioenergetics in patients with Friedreich's ataxia. *Annals of neurology* **49**, 590-596 (2001).
37. C. Mariotti, A. Solari, D. Torta, L. Marano, C. Fiorentini, S. Di Donato, Idebenone treatment in Friedreich patients: one-year-long randomized placebo-controlled trial. *Neurology* **60**, 1676-1679 (2003).

38. V. Libri, C. Yandim, S. Athanasopoulos, N. Loyse, T. Natisvili, P. P. Law, P. K. Chan, T. Mohammad, M. Mauri, K. T. Tam, J. Leiper, S. Piper, A. Ramesh, M. H. Parkinson, L. Huson, P. Giunti, R. Festenstein, Epigenetic and neurological effects and safety of high-dose nicotinamide in patients with Friedreich's ataxia: an exploratory, open-label, dose-escalation study. *Lancet* **384**, 504-513 (2014).
39. M. Perdomini, B. Belbellaa, L. Monassier, L. Reutenauer, N. Messaddeq, N. Cartier, R. G. Crystal, P. Aubourg, H. Puccio, Prevention and reversal of severe mitochondrial cardiomyopathy by gene therapy in a mouse model of Friedreich's ataxia. *Nature medicine* **20**, 542-547 (2014).
40. C. J. Rocca, S. M. Goodman, J. N. Dulin, J. H. Haquang, I. Gertsman, J. Blondelle, J. L. M. Smith, C. J. Heyser, S. Cherqui, Transplantation of wild-type mouse hematopoietic stem and progenitor cells ameliorates deficits in a mouse model of Friedreich's ataxia. *Science translational medicine* **9**, (2017).
41. L. Li, M. Matsui, D. R. Corey, Activating frataxin expression by repeat-targeted nucleic acids. *Nature communications* **7**, 10606 (2016).
42. P. Chapdelaine, C. Gerard, N. Sanchez, K. Cherif, J. Rousseau, D. L. Ouellet, D. Jauvin, J. P. Tremblay, Development of an AAV9 coding for a 3XFLAG-TALEfrat#8-VP64 able to increase in vivo the human frataxin in YG8R mice. *Gene therapy* **23**, 606-614 (2016).
43. D. L. Ouellet, K. Cherif, J. Rousseau, J. P. Tremblay, Deletion of the GAA repeats from the human frataxin gene using the CRISPR-Cas9 system in YG8R-derived cells and mouse models of Friedreich ataxia. *Gene therapy* **24**, 265-274 (2017).
44. B. Santiago-Gonzalez, A. Monguzzi, J. M. Azpiroz, M. Prato, S. Erratico, M. Campione, R. Lorenzi, J. Pedrini, C. Santambrogio, Y. Torrente, F. De Angelis, F. Meinardi, S. Brovelli,

- Permanent excimer superstructures by supramolecular networking of metal quantum clusters. *Science* **353**, 571-575 (2016).
45. B. Santiago-Gonzalez, A. Monguzzi, M. Caputo, C. Villa, M. Prato, C. Santambrogio, Y. Torrente, F. Meinardi, S. Brovelli, Metal Nanoclusters with Synergistically Engineered Optical and Buffering Activity of Intracellular Reactive Oxygen Species by Compositional and Supramolecular Design. *Scientific reports* **7**, 5976 (2017).
46. Y. Gao, N. Shao, Y. Pei, Z. Chen, X. C. Zeng, Catalytic activities of subnanometer gold clusters (Au(1)(6)-Au(1)(8), Au(2)(0), and Au(2)(7)-Au(3)(5)) for CO oxidation. *ACS nano* **5**, 7818-7829 (2011).
47. P. Khandelwal, P. Poddar, Fluorescent metal quantum clusters: an updated overview of the synthesis, properties, and biological applications. *Journal of materials chemistry. B* **5**, 9055-9084 (2017).
48. Z. Q. Jiang, W. H. Zhang, L. Jin, X. Yang, F. Q. Xu, J. F. Zhu, W. X. Huang, Direct XPS evidence for charge transfer from a reduced rutile TiO₂(110) surface to Au clusters. *J Phys Chem C* **111**, 12434-12439 (2007).
49. S. Kim, M. Fujitsuka, T. Majima, Photochemistry of singlet oxygen sensor green. *The journal of physical chemistry. B* **117**, 13985-13992 (2013).
50. M. C. DeRosa, R. J. Crutchley, Photosensitized singlet oxygen and its applications. *Coordin Chem Rev* **233**, 351-371 (2002).
51. S. Goldstein, D. Aschengrau, Y. Diamant, J. Rabani, Photolysis of aqueous H₂O₂: quantum yield and applications for polychromatic UV actinometry in photoreactors. *Environmental science & technology* **41**, 7486-7490 (2007).

52. K. Akasaka, T. Suzuki, H. Ohru, H. Meguro, Study on Aromatic Phosphines for Novel Fluorometry of Hydroperoxides .2. The Determination of Lipid Hydroperoxides with Diphenyl-1-Pyrenylphosphine. *Anal Lett* **20**, 797-807 (1987).
53. S. Yamazoe, K. Koyasu, T. Tsukuda, Nonscalable Oxidation Catalysis of Gold Clusters. *Accounts Chem Res* **47**, 816-824 (2014).
54. Q. Li, W. B. Gao, X. P. Zhang, H. T. Liu, M. L. Dou, Z. P. Zhang, F. Wang, Mesoporous NiO nanosphere: a sensitive strain sensor for determination of hydrogen peroxide. *Rsc Adv* **8**, 13401-13407 (2018).
55. R. Abeti, A. Baccaro, N. Esteras, P. Giunti, Novel Nrf2-Inducer Prevents Mitochondrial Defects and Oxidative Stress in Friedreich's Ataxia Models. *Frontiers in cellular neuroscience* **12**, (2018).
56. F. Lupoli, T. Vannocci, G. Longo, N. Niccolai, A. Pastore, The role of oxidative stress in Friedreich's ataxia. *FEBS letters* **592**, 718-727 (2018).
57. H. Puccio, M. Koenig, The molecular pathogenesis of Friedreich ataxia. *Clin Neurosci Res* **1**, 127-133 (2001).
58. Y. Shidara, P. J. Hollenbeck, Defects in Mitochondrial Axonal Transport and Membrane Potential without Increased Reactive Oxygen Species Production in a Drosophila Model of Friedreich Ataxia. *J Neurosci* **30**, 11369-11378 (2010).
59. K. C. Chen, T. S. Y. Ho, G. Lin, K. L. Tian, M. N. Rasband, H. J. Bellen, Loss of Frataxin activates the iron/sphingolipid/PDK1/Mef2 pathway in mammals. *Elife* **5**, (2016).
60. K. C. Chen, G. Lin, N. A. Haelterman, T. S. Y. Ho, T. C. Li, Z. H. Li, L. Duraine, B. H. Graham, M. Jaiswal, S. Yamamoto, M. N. Rasband, H. J. Bellen, Loss of Frataxin induces iron toxicity, sphingolipid synthesis, and Pdk1/Mef2 activation, leading to neurodegeneration. *Elife* **5**, (2016).

61. M. Dominici, K. Le Blanc, I. Mueller, I. Slaper-Cortenbach, F. C. Marini, D. S. Krause, R. J. Deans, A. Keating, D. J. Prockop, E. M. Horwitz, Minimal criteria for defining multipotent mesenchymal stromal cells. The International Society for Cellular Therapy position statement. *Cytotherapy* **8**, 315-317 (2006).
62. M. Pandolfo, A. Pastore, The pathogenesis of Friedreich ataxia and the structure and function of frataxin. *Journal of neurology* **256 Suppl 1**, 9-17 (2009).
63. J. Bridwell-Rabb, N. G. Fox, C. L. Tsai, A. M. Winn, D. P. Barondeau, Human frataxin activates Fe-S cluster biosynthesis by facilitating sulfur transfer chemistry. *Biochemistry* **53**, 4904-4913 (2014).
64. A. Parent, X. Elduque, D. Cornu, L. Belot, J. P. Le Caer, A. Grandas, M. B. Toledano, B. D'Autreaux, Mammalian frataxin directly enhances sulfur transfer of NFS1 persulfide to both ISCU and free thiols. *Nature communications* **6**, 5686 (2015).
65. C. L. Tsai, D. P. Barondeau, Human frataxin is an allosteric switch that activates the Fe-S cluster biosynthetic complex. *Biochemistry* **49**, 9132-9139 (2010).
66. S. Frank, Dysregulation of mitochondrial fusion and fission: an emerging concept in neurodegeneration. *Acta neuropathologica* **111**, 93-100 (2006).
67. Y. Ikeda, S. Sciarretta, N. Nagarajan, S. Rubattu, M. Volpe, G. Frati, J. Sadoshima, New insights into the role of mitochondrial dynamics and autophagy during oxidative stress and aging in the heart. *Oxidative medicine and cellular longevity* **2014**, 210934 (2014).
68. O. Edenharter, S. Schneuwly, J. A. Navarro, Mitofusin-Dependent ER Stress Triggers Glial Dysfunction and Nervous System Degeneration in a Drosophila Model of Friedreich's Ataxia. *Frontiers in molecular neuroscience* **11**, 38 (2018).

69. N. Calmels, S. Schmucker, M. Wattenhofer-Donze, A. Martelli, N. Vaucamps, L. Reutenauer, N. Messaddeq, C. Bouton, M. Koenig, H. Puccio, The First Cellular Models Based on Frataxin Missense Mutations That Reproduce Spontaneously the Defects Associated with Friedreich Ataxia. *PloS one* **4**, (2009).
70. P. M. Vyas, W. J. Tomamichel, P. M. Pride, C. M. Babbey, Q. Wang, J. Mercier, E. M. Martin, R. M. Payne, A TAT-frataxin fusion protein increases lifespan and cardiac function in a conditional Friedreich's ataxia mouse model. *Human molecular genetics* **21**, 1230-1247 (2012).
71. G. Twig, A. Elorza, A. J. Molina, H. Mohamed, J. D. Wikstrom, G. Walzer, L. Stiles, S. E. Haigh, S. Katz, G. Las, J. Alroy, M. Wu, B. F. Py, J. Yuan, J. T. Deeney, B. E. Corkey, O. S. Shirihai, Fission and selective fusion govern mitochondrial segregation and elimination by autophagy. *The EMBO journal* **27**, 433-446 (2008).
72. I. Tanida, T. Ueno, E. Kominami, LC3 conjugation system in mammalian autophagy. *The international journal of biochemistry & cell biology* **36**, 2503-2518 (2004).
73. N. Mizushima, B. Levine, Autophagy in mammalian development and differentiation. *Nature cell biology* **12**, 823-830 (2010).
74. G. Bjorkoy, T. Lamark, A. Brech, H. Outzen, M. Perander, A. Overvatn, H. Stenmark, T. Johansen, p62/SQSTM1 forms protein aggregates degraded by autophagy and has a protective effect on huntingtin-induced cell death. *The Journal of cell biology* **171**, 603-614 (2005).
75. D. J. Klionsky, et al. Guidelines for the use and interpretation of assays for monitoring autophagy. *Autophagy* **8**, 445-544 (2012).
76. Q. Ma, Role of nrf2 in oxidative stress and toxicity. *Annual review of pharmacology and toxicology* **53**, 401-426 (2013).

77. M. Komatsu, H. Kurokawa, S. Waguri, K. Taguchi, A. Kobayashi, Y. Ichimura, Y. S. Sou, I. Ueno, A. Sakamoto, K. I. Tong, M. Kim, Y. Nishito, S. Iemura, T. Natsume, T. Ueno, E. Kominami, H. Motohashi, K. Tanaka, M. Yamamoto, The selective autophagy substrate p62 activates the stress responsive transcription factor Nrf2 through inactivation of Keap1. *Nature cell biology* **12**, 213-223 (2010).
78. A. Jain, T. Lamark, E. Sjøttem, K. B. Larsen, J. A. Awuh, A. Overvatn, M. McMahon, J. D. Hayes, T. Johansen, p62/SQSTM1 is a target gene for transcription factor NRF2 and creates a positive feedback loop by inducing antioxidant response element-driven gene transcription. *The Journal of biological chemistry* **285**, 22576-22591 (2010).
79. H. Koutnikova, V. Campuzano, M. Koenig, Maturation of wild-type and mutated frataxin by the mitochondrial processing peptidase. *Human molecular genetics* **7**, 1485-1489 (1998).
80. X. Yao, X. Jing, J. Guo, K. Sun, Y. Deng, Y. Zhang, F. Guo, Y. Ye, Icariin Protects Bone Marrow Mesenchymal Stem Cells Against Iron Overload Induced Dysfunction Through Mitochondrial Fusion and Fission, PI3K/AKT/mTOR and MAPK Pathways. *Frontiers in pharmacology* **10**, 163 (2019).
81. Y. Zhang, W. Zhai, M. Zhao, D. Li, X. Chai, X. Cao, J. Meng, J. Chen, X. Xiao, Q. Li, J. Mu, J. Shen, A. Meng, Effects of iron overload on the bone marrow microenvironment in mice. *PloS one* **10**, e0120219 (2015).
82. B. D'Autreaux, M. B. Toledano, ROS as signalling molecules: mechanisms that generate specificity in ROS homeostasis. *Nature reviews. Molecular cell biology* **8**, 813-824 (2007).
83. N. Di Marzo, E. Chisci, R. Giovannoni, The Role of Hydrogen Peroxide in Redox-Dependent Signaling: Homeostatic and Pathological Responses in Mammalian Cells. *Cells* **7**, (2018).

84. P. Mondola, S. Damiano, A. Sasso, M. Santillo, The Cu, Zn Superoxide Dismutase: Not Only a Dismutase Enzyme. *Frontiers in physiology* **7**, 594 (2016).
85. J. D. Aguirre, V. C. Culotta, Battles with iron: manganese in oxidative stress protection. *The Journal of biological chemistry* **287**, 13541-13548 (2012).
86. J. M. Flynn, S. Melov, SOD2 in mitochondrial dysfunction and neurodegeneration. *Free radical biology & medicine* **62**, 4-12 (2013).
87. K. Chantrel-Groussard, V. Geromel, H. Puccio, M. Koenig, A. Munnich, A. Rotig, P. Rustin, Disabled early recruitment of antioxidant defenses in Friedreich's ataxia. *Human molecular genetics* **10**, 2061-2067 (2001).
88. R. Dey, K. Kemp, E. Gray, C. Rice, N. Scolding, A. Wilkins, Human mesenchymal stem cells increase anti-oxidant defences in cells derived from patients with Friedreich's ataxia. *Cerebellum* **11**, 861-871 (2012).
89. M. Reers, S. T. Smiley, C. Mottola-Hartshorn, A. Chen, M. Lin, L. B. Chen, Mitochondrial membrane potential monitored by JC-1 dye. *Methods in enzymology* **260**, 406-417 (1995).
90. S. Al-Mahdawi, R. M. Pinto, D. Varshney, L. Lawrence, M. B. Lowrie, S. Hughes, Z. Webster, J. Blake, J. M. Cooper, R. King, M. A. Pook, GAA repeat expansion mutation mouse models of Friedreich ataxia exhibit oxidative stress leading to progressive neuronal and cardiac pathology. *Genomics* **88**, 580-590 (2006).
91. D. V. Haute, J. M. Berlin, Challenges in realizing selectivity for nanoparticle biodistribution and clearance: lessons from gold nanoparticles. *Therapeutic delivery* **8**, 763-774 (2017).
92. V. Chandran, K. Gao, V. Swarup, R. Versano, H. Dong, M. C. Jordan, D. H. Geschwind, Inducible and reversible phenotypes in a novel mouse model of Friedreich's Ataxia. *Elife* **6**, (2017).

93. L. Nogueira, I. Ramirez-Sanchez, G. A. Perkins, A. Murphy, P. R. Taub, G. Ceballos, F. J. Villarreal, M. C. Hogan, M. H. Malek, (-)-Epicatechin enhances fatigue resistance and oxidative capacity in mouse muscle. *The Journal of physiology* **589**, 4615-4631 (2011).
94. K. Aquilano, P. Vigilanza, S. Baldelli, B. Pagliei, G. Rotilio, M. R. Ciriolo, Peroxisome proliferator-activated receptor gamma co-activator 1alpha (PGC-1alpha) and sirtuin 1 (SIRT1) reside in mitochondria: possible direct function in mitochondrial biogenesis. *The Journal of biological chemistry* **285**, 21590-21599 (2010).
95. A. Safdar, J. P. Little, A. J. Stokl, B. P. Hettinga, M. Akhtar, M. A. Tarnopolsky, Exercise increases mitochondrial PGC-1alpha content and promotes nuclear-mitochondrial cross-talk to coordinate mitochondrial biogenesis. *The Journal of biological chemistry* **286**, 10605-10617 (2011).
96. K. Aquilano, S. Baldelli, B. Pagliei, M. R. Ciriolo, Extranuclear localization of SIRT1 and PGC-1alpha: an insight into possible roles in diseases associated with mitochondrial dysfunction. *Current molecular medicine* **13**, 140-154 (2013).
97. G. Coppola, D. Marmolino, D. Lu, Q. Wang, M. Cnop, M. Rai, F. Acquaviva, S. Coccozza, M. Pandolfo, D. H. Geschwind, Functional genomic analysis of frataxin deficiency reveals tissue-specific alterations and identifies the PPARgamma pathway as a therapeutic target in Friedreich's ataxia. *Human molecular genetics* **18**, 2452-2461 (2009).
98. R. Calvani, A. M. Joseph, P. J. Adihetty, A. Miccheli, M. Bossola, C. Leeuwenburgh, R. Bernabei, E. Marzetti, Mitochondrial pathways in sarcopenia of aging and disuse muscle atrophy. *Biological chemistry* **394**, 393-414 (2013).
99. G. K. Sakellariou, T. Pearson, A. P. Lightfoot, G. A. Nye, N. Wells, Giakoumaki, II, A. Vasilaki, R. D. Griffiths, M. J. Jackson, A. McArdle, Mitochondrial ROS regulate oxidative damage and mitophagy but not age-related muscle fiber atrophy. *Scientific reports* **6**, 33944 (2016).

100. G. Favaro, V. Romanello, T. Varanita, M. Andrea Desbats, V. Morbidoni, C. Tezze, M. Albiero, M. Canato, G. Gherardi, D. De Stefani, C. Mammucari, B. Blaauw, S. Boncompagni, F. Protasi, C. Reggiani, L. Scorrano, L. Salviati, M. Sandri, DRP1-mediated mitochondrial shape controls calcium homeostasis and muscle mass. *Nature communications* **10**, 2576 (2019).
101. J. Woo, J. O. Min, D. S. Kang, Y. S. Kim, G. H. Jung, H. J. Park, S. Kim, H. An, J. Kwon, J. Kim, I. Shim, H. G. Kim, C. J. Lee, B. E. Yoon, Control of motor coordination by astrocytic tonic GABA release through modulation of excitation/inhibition balance in cerebellum. *Proceedings of the National Academy of Sciences of the United States of America* **115**, 5004-5009 (2018).
102. D. Marmolino, F. Acquaviva, M. Pinelli, A. Monticelli, I. Castaldo, A. Filla, S. Coccozza, PPAR-gamma agonist Azelaoyl PAF increases frataxin protein and mRNA expression: new implications for the Friedreich's ataxia therapy. *Cerebellum* **8**, 98-103 (2009).
103. K. C. Kemp, A. J. Cook, J. Redondo, K. M. Kurian, N. J. Scolding, A. Wilkins, Purkinje cell injury, structural plasticity and fusion in patients with Friedreich's ataxia. *Acta neuropathologica communications* **4**, 53 (2016).
104. H. Lin, J. Magrane, E. M. Clark, S. M. Halawani, N. Warren, A. Rattelle, D. R. Lynch, Early VGLUT1-specific parallel fiber synaptic deficits and dysregulated cerebellar circuit in the KIKO mouse model of Friedreich ataxia. *Disease models & mechanisms* **10**, 1529-1538 (2017).
105. M. Vreugdenhil, J. G. Jefferys, M. R. Celio, B. Schwaller, Parvalbumin-deficiency facilitates repetitive IPSCs and gamma oscillations in the hippocampus. *Journal of neurophysiology* **89**, 1414-1422 (2003).
106. B. Molla, F. Riveiro, A. Bolinches-Amoros, D. C. Munoz-Lasso, F. Palau, P. Gonzalez-Cabo, Two different pathogenic mechanisms, dying-back axonal neuropathy and pancreatic senescence, are

present in the YG8R mouse model of Friedreich's ataxia. *Disease models & mechanisms* **9**, 647-657 (2016).

107. M. Igoillo-Esteve, E. Gurgul-Convey, A. Hu, L. Romagueira Bichara Dos Santos, B. Abdulkarim, S. Chintawar, L. Marselli, P. Marchetti, J. C. Jonas, D. L. Eizirik, M. Pandolfo, M. Cnop, Unveiling a common mechanism of apoptosis in beta-cells and neurons in Friedreich's ataxia. *Human molecular genetics* **24**, 2274-2286 (2015).
108. M. Ristow, H. Mulder, D. Pomplun, T. J. Schulz, K. Muller-Schmehl, A. Krause, M. Fex, H. Puccio, J. Muller, F. Isken, J. Spranger, D. Muller-Wieland, M. A. Magnuson, M. Mohlig, M. Koenig, A. F. Pfeiffer, Frataxin deficiency in pancreatic islets causes diabetes due to loss of beta cell mass. *The Journal of clinical investigation* **112**, 527-534 (2003).
109. M. Cnop, M. Igoillo-Esteve, M. Rai, A. Begu, Y. Serroukh, C. Depondt, A. E. Musuaya, I. Marhfour, L. Ladriere, X. Moles Lopez, D. Lefkaditis, F. Moore, J. P. Brion, J. M. Cooper, A. H. Schapira, A. Clark, A. H. Koeppen, P. Marchetti, M. Pandolfo, D. L. Eizirik, F. Fery, Central role and mechanisms of beta-cell dysfunction and death in friedreich ataxia-associated diabetes. *Annals of neurology* **72**, 971-982 (2012).
110. Y. Shan, R. A. Schoenfeld, G. Hayashi, E. Napoli, T. Akiyama, M. Iodi Carstens, E. E. Carstens, M. A. Pook, G. A. Cortopassi, Frataxin deficiency leads to defects in expression of antioxidants and Nrf2 expression in dorsal root ganglia of the Friedreich's ataxia YG8R mouse model. *Antioxidants & redox signaling* **19**, 1481-1493 (2013).
111. M. Zhang, C. An, Y. Gao, R. K. Leak, J. Chen, F. Zhang, Emerging roles of Nrf2 and phase II antioxidant enzymes in neuroprotection. *Progress in neurobiology* **100**, 30-47 (2013).
112. F. Lim, G. M. Palomo, C. Mauritz, A. Gimenez-Cassina, B. Illana, F. Wandosell, J. Diaz-Nido, Functional recovery in a Friedreich's ataxia mouse model by frataxin gene transfer using an HSV-

- 1 amplicon vector. *Molecular therapy : the journal of the American Society of Gene Therapy* **15**, 1072-1078 (2007).
113. W. Chen, Y. Sun, K. Liu, X. Sun, Autophagy: a double-edged sword for neuronal survival after cerebral ischemia. *Neural regeneration research* **9**, 1210-1216 (2014).
114. C. Evangelisti, C. Evangelisti, F. Chiarini, A. Lonetti, F. Buontempo, L. M. Neri, J. A. McCubrey, A. M. Martelli, Autophagy in acute leukemias: a double-edged sword with important therapeutic implications. *Biochimica et biophysica acta* **1853**, 14-26 (2015).
115. H. Chen, A. Chomyn, D. C. Chan, Disruption of fusion results in mitochondrial heterogeneity and dysfunction. *The Journal of biological chemistry* **280**, 26185-26192 (2005).
116. H. Chen, J. M. McCaffery, D. C. Chan, Mitochondrial fusion protects against neurodegeneration in the cerebellum. *Cell* **130**, 548-562 (2007).
117. R. Scherz-Shouval, E. Shvets, E. Fass, H. Shorer, L. Gil, Z. Elazar, Reactive oxygen species are essential for autophagy and specifically regulate the activity of Atg4. *The EMBO journal* **26**, 1749-1760 (2007).
118. G. Kroemer, G. Marino, B. Levine, Autophagy and the integrated stress response. *Molecular cell* **40**, 280-293 (2010).
119. L. Murrow, J. Debnath, Autophagy as a stress-response and quality-control mechanism: implications for cell injury and human disease. *Annual review of pathology* **8**, 105-137 (2013).
120. A. Puissant, N. Fenouille, P. Auberger, When autophagy meets cancer through p62/SQSTM1. *American journal of cancer research* **2**, 397-413 (2012).
121. M. Z. McMackin, C. K. Henderson, G. A. Cortopassi, Neurobehavioral deficits in the KIKO mouse model of Friedreich's ataxia. *Behavioural brain research* **316**, 183-188 (2017).

122. J. P. Dougherty, D. A. Springer, M. C. Gershengorn, The Treadmill Fatigue Test: A Simple, High-throughput Assay of Fatigue-like Behavior for the Mouse. *Journal of visualized experiments : JoVE*, (2016).
123. I. Rattray, E. Smith, R. Gale, K. Matsumoto, G. P. Bates, M. Modo, Correlations of behavioral deficits with brain pathology assessed through longitudinal MRI and histopathology in the R6/2 mouse model of HD. *PloS one* **8**, e60012 (2013).
124. K. C. Kemp, N. Cerminara, K. Hares, J. Redondo, A. J. Cook, H. R. Haynes, B. R. Burton, M. Pook, R. Apps, N. J. Scolding, A. Wilkins, Cytokine therapy-mediated neuroprotection in a Friedreich's ataxia mouse model. *Annals of neurology* **81**, 212-226 (2017).
125. A. Farini, C. Sitzia, L. Cassinelli, F. Colleoni, D. Parolini, U. Giovanella, S. Maciotta, A. Colombo, M. Meregalli, Y. Torrente, Inositol 1,4,5-trisphosphate (IP3)-dependent Ca²⁺ signaling mediates delayed myogenesis in Duchenne muscular dystrophy fetal muscle. *Development* **143**, 658-669 (2016).

Acknowledgements

We thank Claudia V. Pereira (Carlos T. Moraes Lab., University of Miami) for advice and help with Seahorse Oxygen flow, Paolo E. Porporato (MBC, Turin, Italy) for critical reading of the manuscript. This research was funded by Associazione “OGNI GIORNO” – per Emma – Onlus (Treviso, Italy) and Associazione per il sorriso di Ilaria di Montebruno Onlus (Genova, Italy). Funders of the study had no role in study design, data analysis, data interpretation, or writing of the report.

Author contributions

C.V. and Y.T. conceived and designed the experiments. C.V., Y.T., and G.R.M. wrote the paper. C.V., A.U., M.L., C.R., R.J., A.B., B.M., M.B., C.M., I.F., D.B., M.B., G.F., M.P., T.A., R.R., C.T.M., A.M., G.R.M., and Y.T., performed the experiments and acquired the data. C.V., A.M., G.R.M., C.T.M., and Y.T. interpreted and analyzed the data. All the authors stated were involved in the critical revision of the manuscript and approved the final version of the article, including the authorship list. The corresponding author had full access to all the data in the study and had final responsibility for the decision to submit for publication.

Conflict of interest

C.V., A.M., and Y.T. are listed as inventors on a patent application (n. IT102019000020724) for Au₈-pXs mediated therapy for FRDA. A.U., M.L., C.R., R.J., A.B., B.M., M.B., C.M., I.F., D.B., M.P., T.A., R.R., C.T.M., G.R.M., declare no competing interests.

Figure legends

Fig.1. Molecular structure and scavenger abilities of the Au₈ gold clusters superstructures (Au₈-pXs)

(A) Absorption and photoluminescence (PL) spectrum of networked gold quantum clusters Au₈-pX in HPLC water dispersion. The inset is a sketch of the Au₈-pX molecular structure. (B) Relative singlet oxygen (¹O₂^{*}) concentration as a function of time in HPLC water using rose bengal (RB, 5 μM) as photosensitizer and SOSGTM (10 μg mL⁻¹) as molecular optical probe for ¹O₂^{*}. The relative increment is monitored in presence (dots) and in absence (crosses) of Au₈-pX (175 μM). Control experiments are performed without photosensitizer (triangles) and with SOSGTM alone (squares). (C) Relative superoxide (O₂^{•-}) concentration as a function of time in PBS:H₂O₂ solution under UV excitation, using MitoSOXTM red (15 μg mL⁻¹) as optical probe for O₂^{•-}. The relative increment is monitored in presence (dots) and in absence (crosses) of Au₈-pX (175 μM). (D) Relative hydrogen peroxide (H₂O₂) concentration as a function of time in PBS solution measured using diphenyl-1-pyrenylphosphine (DPPP, 1.5×10⁻⁵ M) as molecular optical probe for H₂O₂. The H₂O₂ concentration has been varied by progressively adding it to the solution. The effective relative increment of H₂O₂ is monitored in presence (dots) and in absence (crosses) of Au₈-pX (50 μM). (E-F) Cyclic voltammetry of a PBS (solid line) and a PBS: H₂O₂ solution (1:2 in volume, dots) in absence (E) and in presence (F) of Au₈-pX (350 μM).

Fig.2. Au₈-pX modulation of the autophagy pathway in FRDA derived BMSCs

(A) Representative confocal images of mitochondria in BMSCs derived from FRDA#1 (BMSCs^{FRDA#1}) and FRDA#2 (BMSCs^{FRDA#2}) patients stained with MitoTrackerTM Red CMXRos. Scale bars, 25 μm. (B) Representative confocal images of BMSCs derived from FRDA#1 and #2 patients

labeled with 10 μ M Au₈-pXs for 24 hours and stained with MitoTrackerTM Red CMXRos. Au₈-pXs were excited with 405nm UV/Vis and emitted fluorescence was collected between 500 and 540 nm. Scale bars, 10 μ m. Lower panel depicts heatmap images of colocalization (yellow) of mitochondrial staining and Au₈-pXs through EZColocalization plugin of ImageJ software. Scale bars, 5 μ m. (C) Representative western blots of frataxin and FXN related proteins (Nrf2, NFS1), mitochondrial fusion (Mfn1) and fission (Drp1) proteins, and proteins related to the autophagic flux (LC3I, LC3II, p62, and Atg7) in Au₈-pXs treated and untreated (nt) BMSCs^{FRDA}. BMSCs from age matched healthy donors (CTR#1 and CTR#2) were evaluated as controls. Actin was used as loading control. (D) Representative western blot quantification of protein bands in Au₈-pXs treated and untreated (nt) BMSCs^{FRDA} and age matched BMSCs^{CTR}. Data were expressed as means \pm SD of 2-4 independent experiments; * P<0.05, ** P<0.01, *** P<0.001, **** P<0.0001 (ordinary one-way ANOVA, Bonferroni's test).

Fig.3. Recovery of the mitochondrial bioenergetic function in FRDA derived BMSCs treated with Au₈-pXs.

(A) Incucytes[®] evaluation of proliferative capacities in 5 and 10 μ M Au₈-pXs treated BMSCs^{FRDA#1}, BMSCs^{FRDA#1}, and BMSC^{CTR}. Recording of object count/mm² was performed every 6 hours from Au₈-pX labeling of cells (hour 0) up to 48 hours. Data were expressed as means \pm SD of 3 independent experiments. Statistical analysis was performed by ordinary two-way ANOVA, followed by post hoc Bonferroni's test; * P<0.05, ** P<0.01, *** P<0.001, **** P<0.0001. (B) Assessment of ROS in BMSCs^{FRDA#1} treated for 24 hours with 5 and 10 μ M Au₈-pXs, untreated BMSCs^{FRDA#1}, and BMSCs^{CTR}. Data were expressed as means \pm SD of 3 independent experiments; ** P<0.01, **** P<0.0001 (ordinary one-way ANOVA, Bonferroni's test). (C) Mitochondrial analysis of oxygen consumption rates (OCR) and extracellular acidification rates (ECAR) in Au₈-pXs treated and untreated

BMSCs^{FRDA#1} measured by XFp Extracellular Flux Analyzer Seahorse. Cells were subsequently treated with 2.5 μ M Oligomycin (Olig), 0.5 μ M FCCP and 1 μ M rotenone and antimycin (R/A). N=6 measurements were recorded before each treatment. **(D)** OCR measures were used to calculate non-mitochondrial respiration, basal and maximal respiratory capacity, as well as ATP production and spare respiratory capacity. **(C-D)** Data were expressed as means \pm SD of n=3 wells per cell group (3 independent experiments); * P<0.05, ** P<0.01, *** P<0.001, **** P<0.0001 (ordinary two-way ANOVA, Bonferroni's test). **(E)** Mitochondrial membrane potential (MMP) evaluation by the lipophilic dye JC-1. Statistical analysis of red/green ratio (green: monomeric form; red: aggregate) of fluorescence variation. Data were expressed as means \pm SD of n=3 wells per cell group (3-5 independent experiments); * P<0.05, ** P<0.01, *** P<0.001, **** P<0.0001 (ordinary one-way ANOVA, Bonferroni's test).

Fig.4. Au₈pX engraftment in skeletal and cardiac muscles of treated YG8sR mice

(A) Schematic of Au₈pX intravenous injection into 12 months old YG8sR mice (Au₈pX YG8sR; n=10) and functional measurement evaluation time points. Untreated YG8sR mice (n=10) were examined at the same time points. **(B)** Treadmill performance of Au₈pX YG8sR (n=6) and YG8sR (n=4) mice for three different experimental conditions: low intensity (38cm/sec), medium intensity (42cm/sec), and high intensity (46 cm/sec). Results from the onset of pathological signs (B.I.) to the sacrifice day were displayed and expressed as averaged number of shocks \pm SD. **(C)** Outcomes from grip strength test 60 and 180 days after Au₈pX injection (n=4 per group). Data were expressed as means \pm SD. **(D-E)** % of ejection fraction (EF) and fractional shortening (FS) was calculated from echocardiography images performed on Au₈pX YG8sR (n=6) and YG8sR (n=4) mice before the sacrifice. %EF and FS were expressed as means \pm SD. Other echocardiography measures were acquired and expressed as ratio of Au₈pX YG8sR and YG8sR values. **(B to D)** Statistical analyses were performed with ordinary two-way

ANOVA followed by Bonferroni's test; * $P < 0.05$, ** $P < 0.01$, *** $P < 0.001$, **** $P < 0.0001$. **(F)** Representative western blots of frataxin and FXN related proteins (Nrf2, NFS1, PGC-1 α and PPAR γ) and proteins related to the autophagic flux (LC3I, LC3II, p62, and Atg7) in QAs and hearts of Au₈-pX YG8sR and YG8sR mice. Vinculin was used as loading control. Data were expressed as means \pm SD of 2-4 independent experiments. **(G)** Representative images of QAs and hearts from Au₈-pX YG8sR and YG8sR mice stained with Azan Mallory for fibrosis detection. Scale bars, 200 μ m. Tissue fibrosis in QAs and hearts and QA myofiber area (μ m²) was quantified by Threshold color Plugin of ImageJ Software (n=50 images for each mouse). Data were represented as box and whisker plots: boxes indicate 25th to 75th percentiles and whisker extending from the minimum to maximum values; lines indicate median. **(H)** Representative western blots of fibrotic markers in hearts of Au₈-pX YG8sR and YG8sR mice. Vinculin was used as loading control. Data were expressed as means \pm SD of 2-4 independent experiments. **(I)** Electron microscopy images of thin sections from QAs of Au₈-pX YG8sR and YG8sR mice. Scale bar, 2 μ m.

Fig.5. Au₈-pX engraftment in nervous systems of treated YG8sR mice

(A) Schematic of Au₈-pXs intravenous injection into 12 months old YG8sR mice and functional measurement time points. **(B)** Stride length and width from foot print tests performed on Au₈-pX YG8sR (n=5) and YG8sR (n=5) mice after 60, 120 and 180 days from Au₈-pX injection. **(C)** Rotarod balance coordination of Au₈-pXs injected YG8sR (n=5) and YG8sR (n=3) mice from the onset of pathological signs (B.I.) to the sacrifice day. **(B-C)** Data were expressed as means \pm SD; * $P < 0.05$, ** $P < 0.01$, *** $P < 0.001$, **** $P < 0.0001$ (ordinary two-way ANOVA, Bonferroni's test). **(D)** Representative western blot of frataxin and FXN related proteins (Nrf2, NFS1, PGC-1 α and PPAR γ), proteins related to the autophagic flux (LC3I, LC3II, p62, and Atg7) and Purkinje cells (Parvalbumin and Calbindin-D) in

cerebellum lysates of Au₈pX YG8sR and YG8sR mice. Data were expressed as means \pm SD of 2-4 independent experiments. **(E)** Representative confocal images of cerebella from Au₈pX YG8sR and YG8sR mice stained for Parvalbumin, Calbindin-D, NeuroT, and NeuN for neurons and Purkinje cells, GFAP for microglia, and glutathione peroxidase (GPx-1). Scale bars: 100 μ m for Calbindin-D tile scan, inset magnification 10 μ m; 20 μ m for the other fluorescence staining in **(E)** and **(F)**.

Fig.6. Au₈-pXs treatment restores stress and redox pathways of YG8sR mice

(A) RT-qPCR for Prdx2, Gstm1 and Nrf2 from CNS (cerebellum, cortex, and BGs) and DRGs from of Au₈pX YG8sR and YG8sR mice. Data were expressed as means \pm SD for n=3 independent experiments. All comparisons were performed for each gene with unpaired Student's t-test **(B)** Total and mitochondrial extract analysis of lipid peroxidation and DNA oxidative damages from CNS, hearts and skeletal muscles (QAs, TAs, and SL) of Au₈pX YG8sR and YG8sR mice. **(C)** Glutathione (GSH), Glutathione-S transferase (GST), and oxidized glutathione (GSSG) measurements in total lysates of CNS, hearts and skeletal muscles from Au₈pX YG8sR and YG8sR mice. **(D)** Cytosolic and mitochondrial SOD measurements in CNS, hearts and skeletal muscles from Au₈pX YG8sR and YG8sR mice. **(E)** ATP production and electron transport chain (ETC) flux measurements in mitochondrial extracts of CNS, hearts and skeletal muscles from Au₈pX YG8sR and YG8sR mice. **(B-E)** Data were expressed as means \pm SD for n=3 independent experiments. Statistical analyses were performed by ordinary two-way ANOVA followed by post hoc Bonferroni's test.

Figures

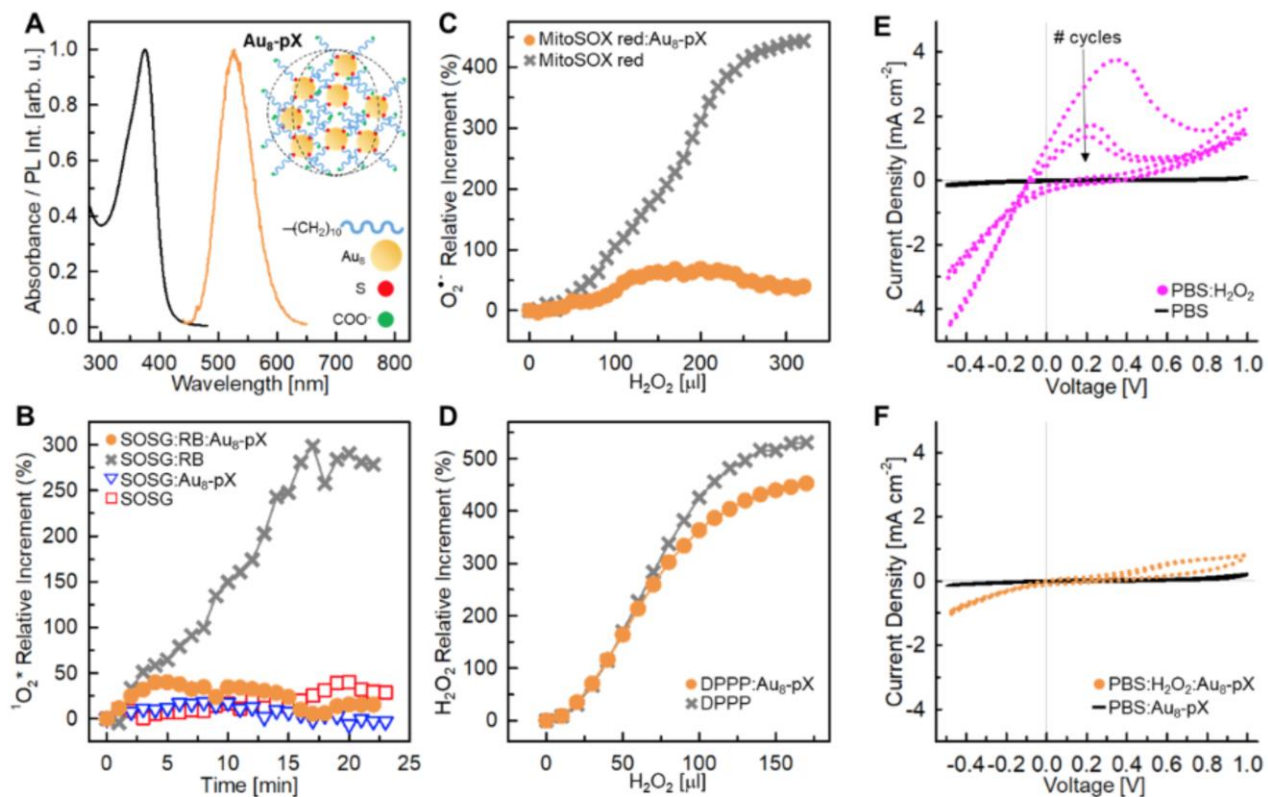


Figure 1

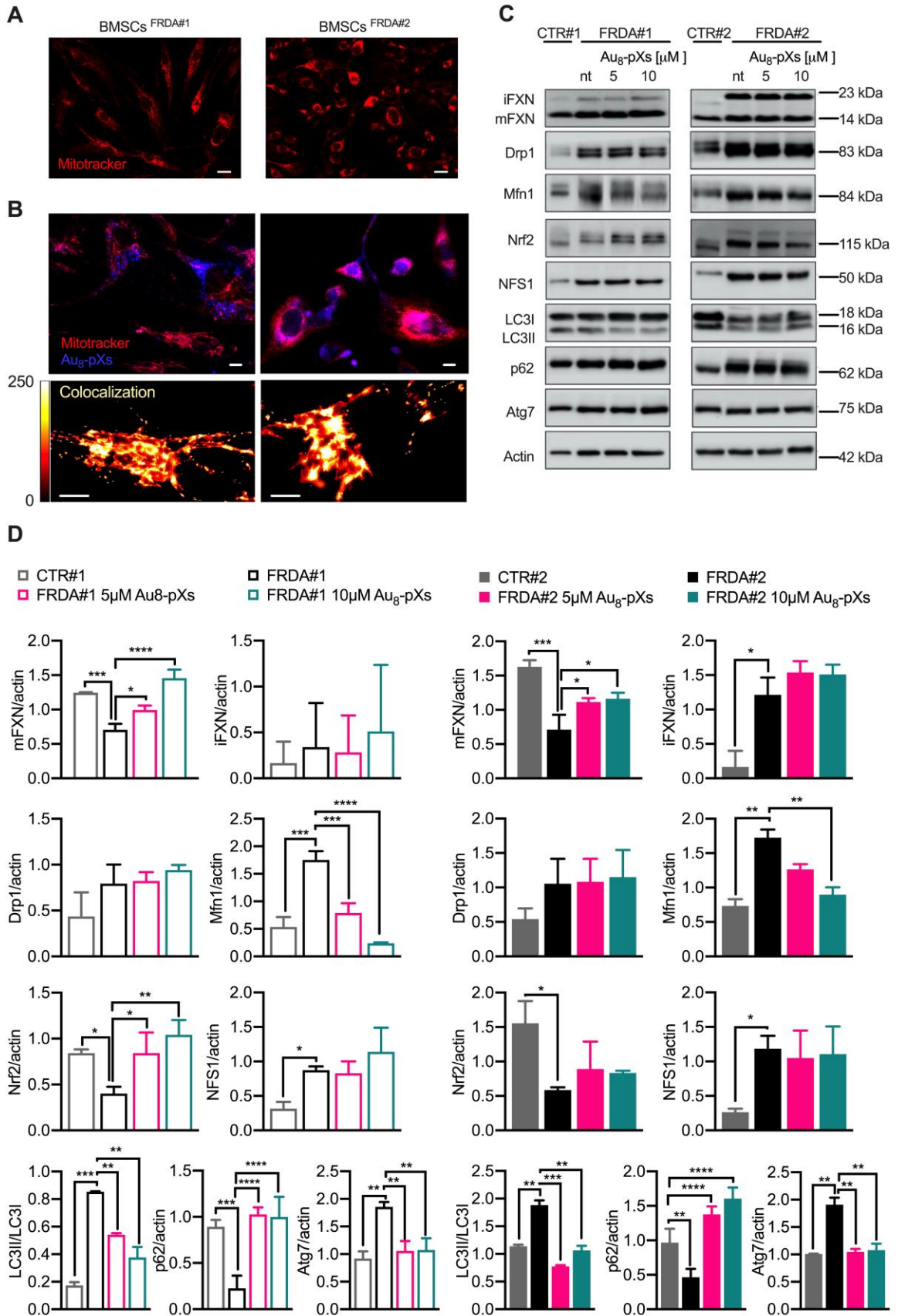


Figure 2

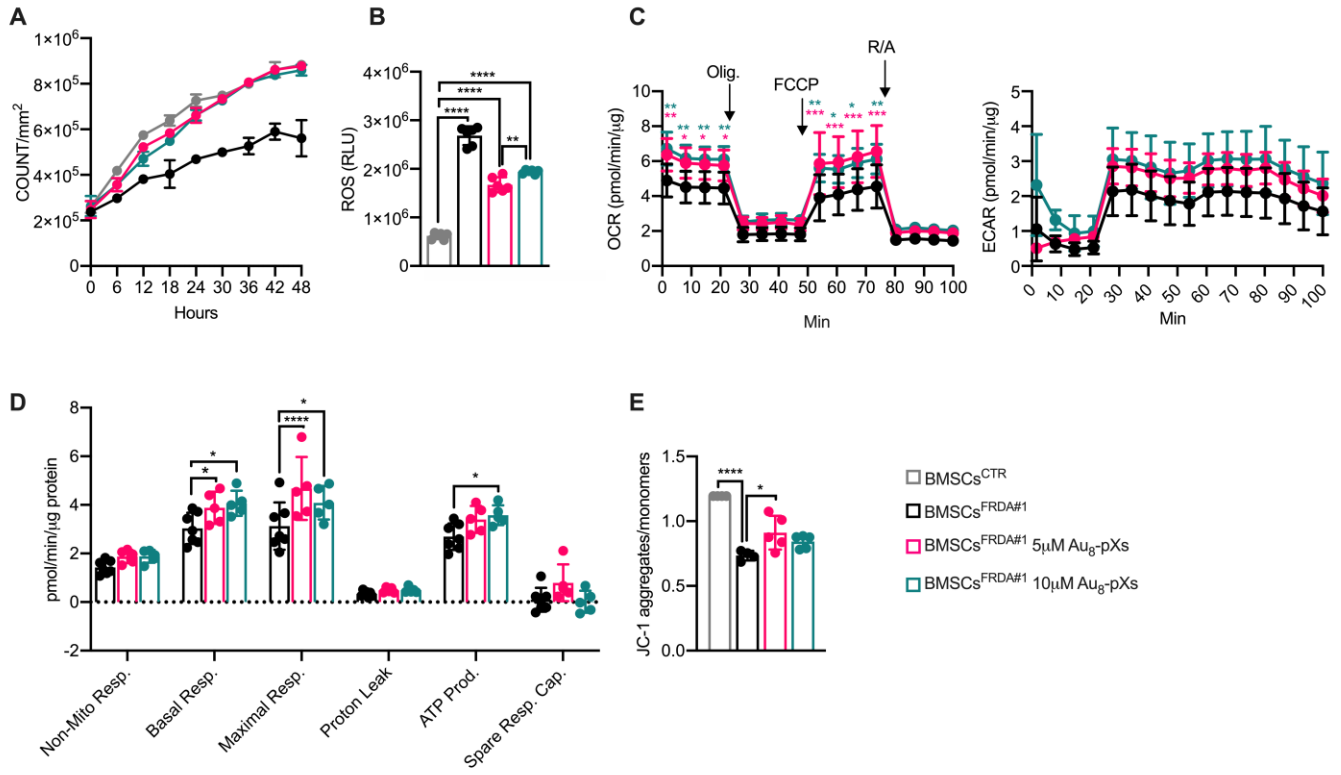


Figure 3

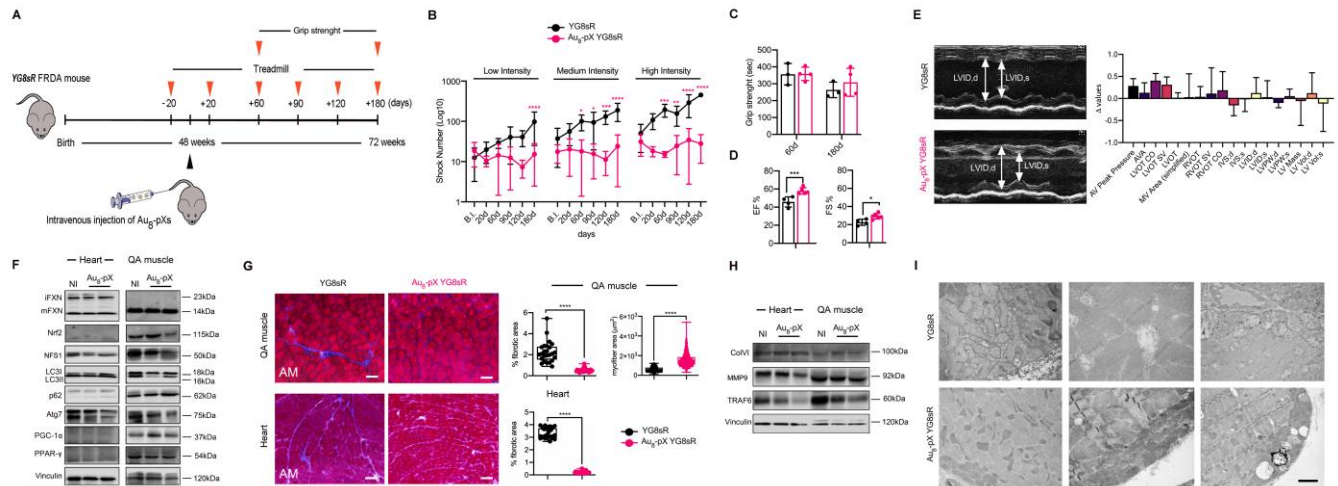


Figure 4

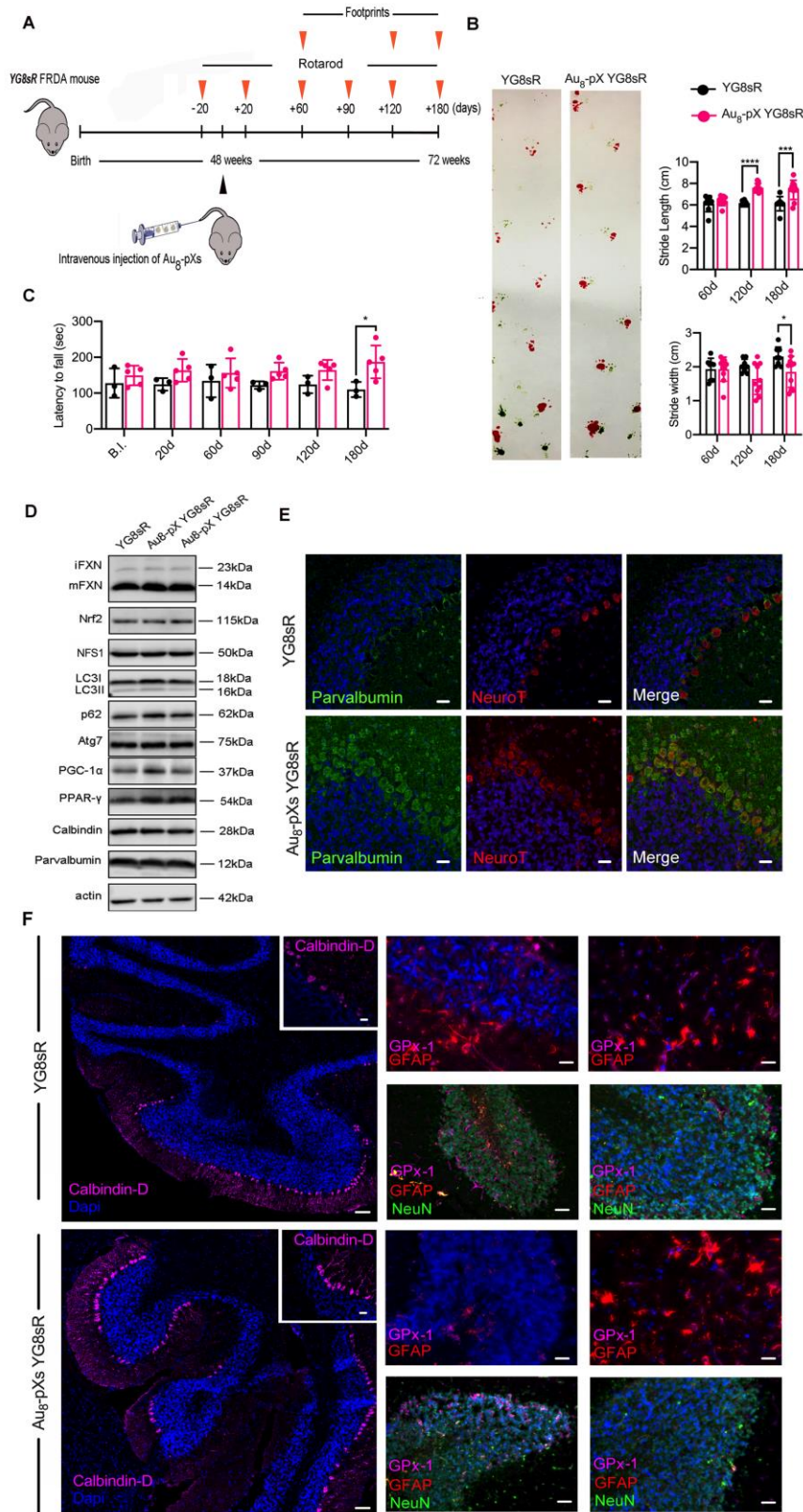


Figure 5

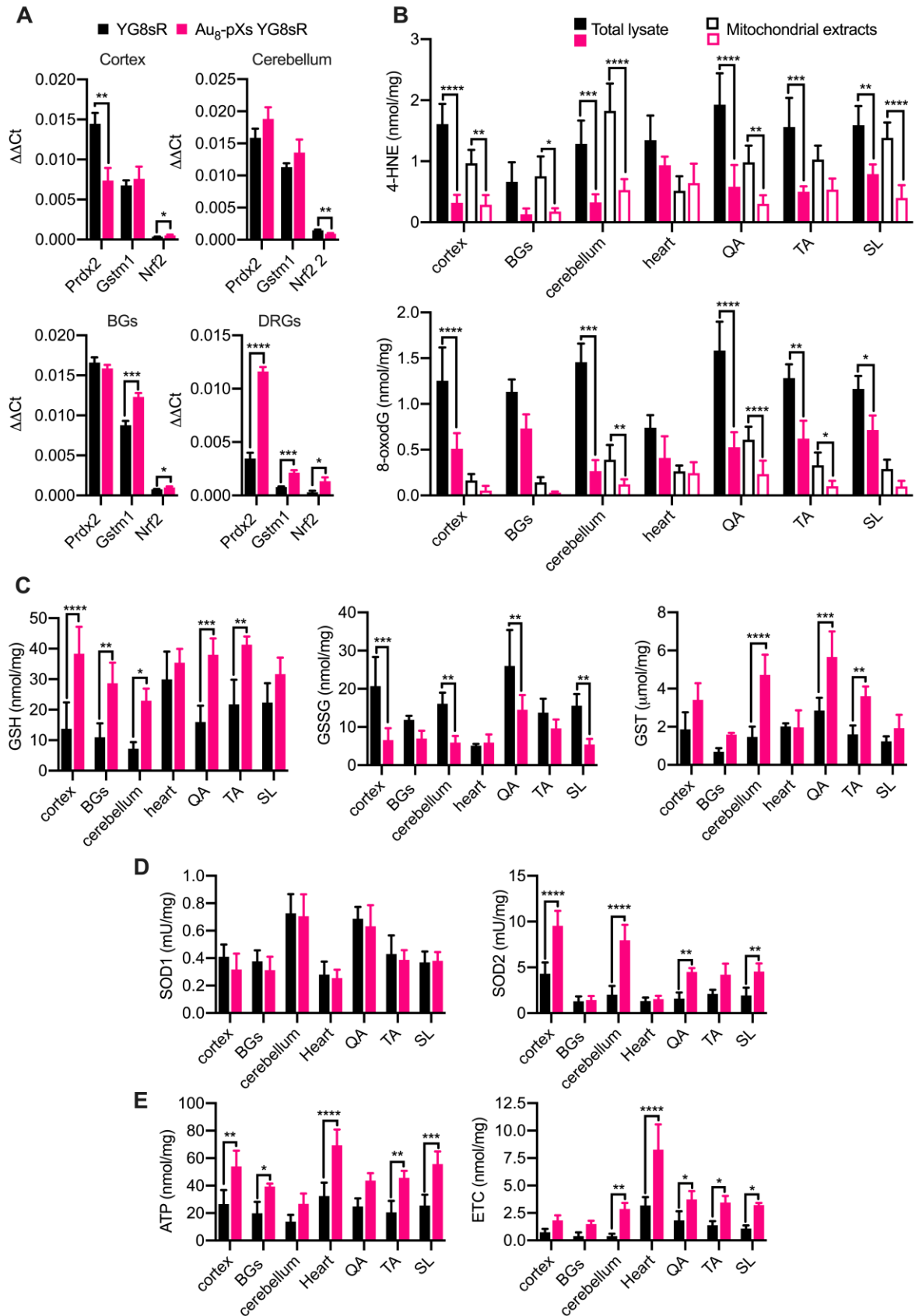


Figure 6

Supplementary Materials

Materials and methods

Evaluation of Au8-pX interactions to reactive oxygen species

Singlet Oxygen ($^1O_2^$) Sensing*

The $^1O_2^*$ species is generated in solution by using the photosensitizer Rose Bengal (RB) under laser excitation at 532 nm (40 mW cm⁻²). As optical probe, we employ the SOSGTM fluorescent probe (Invitrogen-Thermo Fisher Scientific) under laser excitation at 473 nm (9 mW cm⁻²). The intensity of the SOSGTM PL signal that is proportional to the concentration of $^1O_2^*$ in solution is recorded as function of time as described above. 100 µg of SOSGTM have been added to 1 ml di methanol. The obtained solution is dilute five times with HPLC water. The final composition has been obtained by adding 1 ml of Au8-pX (350 µM) in water or 1 ml of pure water H₂O to obtain the same final concentration of SOSG. RB has been added when required in a concentration of 5 µM.

Superoxide ($O_2^{\bullet-}$) sensing

The $O_2^{\bullet-}$ is generate by exploiting the photolysis of H₂O₂ under UV light at 405 nm (10 mW cm⁻²) as described in ref. [*Environ. Sci. Technol.*, vol. 41, no. 21, pp. 7486–7490, 2007]. As optical probe we employ the MitoSOXTM red fluorescent probe (Invitrogen-Thermo Fisher Scientific) under laser excitation at 532 nm (10 mW cm⁻²). The intensity of the MitoSOXTM red PL signal that is proportional to the concentration of $^1O_2^*$ in solution is recorded upon progressive addition of H₂O₂. 50 µg of are dissolved in 5 ml of DMSO:H₂O (10% in volume). For experiments, 1 ml of this solution is mixed with 0.5 ml of pure water without or with Au8-pXs (120 µM). The H₂O₂ has been added to the solution as 10 µL droplets of a H₂O₂:H₂O solution (0.3% in volume). For quantitative relative comparison, the MitoSOXTM red integrated emission intensity has been normalized to the sample absorbance, corrected by the Au8-pXs absorption, and measured after addition of each droplet.

Hydrogen peroxide (H₂O₂) sensing

As optical probe, we employ the diphenyl-1-pyrenylphosphine (DPPP, Invitrogen-Thermo Fisher Scientific). DPPP become fluorescent once oxidized upon interaction with H₂O₂. The oxidized for show absorption in UV-Vis region and an emission peak at 380 nm. The DPPP fluorescence intensity proportional to the H₂O₂ concentration has been monitored upon laser excitation at 355 nm (95 mW cm⁻²) upon progressive addition of H₂O₂. The DPPP is dissolved in ethanol at 100 μM concentration. For experiments, 1.5 ml of DPPP solution are mixed with 0.25 mL of a H₂O₂:water solution (0.003% in volume) with or without of Au₈-pXs (85 μM). H₂O₂ has been added progressively as 10 μL droplets of the initial H₂O₂:water solution.

Cyclic Voltammetry. All the measurements were performed using a potentiostat/galvanostat PARSTAT 2273 (Princeton Applied Research). Cyclic voltammetry is carried out at 50 mV/s in a cell composed by the Au pin as working electrode, Pt flag as counter electrode and SCE as reference electrode. All potentials are reported against SCE. To mimic the biological environment, the measurements were performed in PBS, phosphate-buffered saline, a water solution containing NaCl and Na₂HPO₄ salts in which the buffer keeps a constant pH around 7.4.

Isolation and characterization of BMSCs from FRDA patients.

FRDA patients' and healthy donors' bone marrow (BM) was aspirated from the left posterior iliac crest with local anesthesia in a sterile fashion, eluted through 100μm cell strainer to remove bone spicules, and diluted 1:1(v/v) with DMEM (Gibco-Thermo Fisher Scientific) containing 10% of fetal bovine serum (FBS) (Gibco-Thermo Fisher Scientific) and 0.1% gentamicin (Gibco-Thermo Fisher Scientific). Mononuclear cell (MNC) fraction was separated by density gradient centrifugation. Briefly, 5ml of diluted bone marrow was layered on top of 2.5ml of Lymphoprep™ (STEM CELL

Technologies) and centrifuged at 600 g for 20 minutes at room temperature. MNCs were carefully aspirated and collected into 15ml centrifuge tube with fresh cell culture medium. Total volume of suspended pellet was transferred to a 175 cm² ventilated flask and incubated for 24 hours at 5% CO₂ and 37°C. Medium was then removed, and cells were washed with phosphate buffered saline (PBS) to eliminate non-adherent cells. DMEM/F12 (Thermo Fisher Scientific) with 10% of FBS and 0.1% gentamicin was used for subsequent cultivation of BMSCs and replaced every 3 days. At 90% confluence, BMSCs were treated with trypsin-EDTA (Gibco-Thermo Fisher Scientific), counted, and prepared for further analyses or in vitro culture. FACS analysis of BMSCs from FRDA patients (BMSCs^{FRDA#1}, BMSCs^{FRDA#2}) and a healthy donor (BMSCs^{CTR}) was performed with the Cytomics FC500 (Beckman-Coulter) machine for the expression of mesenchymal markers (CD44, CD73, CD105, and CD90) (Dominici et al. Cytotherapy 2006). Data analyzed with CXP 2.1 software. 10⁵ cells were resuspended in phosphate buffered saline (PBS) and incubated with 10µl primary antibodies anti-CD44-FITC, anti-CD73-APC, anti-CD105-PE, anti-CD90-APC, and anti-7AAD. The 7-AAD was added to exclude non-viable cells from the analysis. Anti-CD34-PERCP and anti-45-APC were used to exclude hematopoietic cells and leukocytes. All the antibodies were purchased from BD Biosciences-Pharmingen. The controls were isotype-matched human immunoglobulins. Incubation was performed at 4°C for 20 minutes. Cells were then washed in PBS with 1% heat-inactivated FCS and 0.1% sodium azide. Each analysis included at least 5-10x10⁴ events for each gate. A light-scatter gate was set up to eliminate cell debris from the analysis. The percentage of positive cells was assessed after correction for the percentage reactive to an isotype control conjugated to relative fluorochromes. Cell proliferative capacity was assessed by MTT experiments, according to manufacturers' instructions. Briefly, BMSCs^{FRDA#1}, BMSCs^{FRDA#2}, and BMSCs^{CTR} were seeded in a 96-well plate at a density of 5000 cells/well, in triplicate. 50µg/ml MTT solution (Methylthiazolyldiphenyl-tetrazolium bromide) (Sigma Aldrich) was added to the samples and

incubated for 4 hours at 37°C. The converted dye was then solubilized with DMSO (Sigma Aldrich) and the absorbance measured at 560nm with GloMax Discover plate reader (Promega). MTT assay was performed 24, 48 and 72 hours after seeding, for three independent experiments.

IncuCytes proliferation assay and ROS detection

Proliferation of BMSCs^{FRDA#1} labeled with Au₈-pXs, BMSCs^{FRDA#1} and BMSCs^{CTR1} seeded into 6-well plates were monitored by the analysis of object count/mm² over time. Data were recorded every 6 hours from Au₈-pX loading (0 hours) up to 48 hours according to the IncuCyte® (Sartorius) manufacturer's instructions. For the evaluation of ROS produced in culture, cells were seeded into a 96-well plate, as described for MTT test. The analysis was performed 24 hours after 5 or 10µM Au₈-pXs labeling by the means of ROS-Glo™ H₂O₂ Assay (Promega) and following the protocol for lytic procedure. As ROS are very sensitive to the in vitro environment and their accurate determination challenging, for this specific assay basal BMSCs medium was replaced with DMEM/F12 without phenol red and HEPES to diminish interferences in measurements. Relative luminescence units were measured by GloMax Discover plate reader. Both IncuCytes and ROS assays were performed in three independent experiments.

Echocardiography

Transthoracic echocardiography was performed with a small animal high-resolution imaging system (VeVo2100, VisualSonics, Inc, Toronto, Canada) equipped with a 22–55 MHz transducer (MicroScan Transducers, MS500D). The mice, anesthetized by isoflurane (2%) inhalation and maintained by mask ventilation (isoflurane 1%), were placed in a shallow left lateral decubitus position, with strict thermoregulation (37 ± 1 °C) to optimize physiological conditions and reduce hemodynamic variability. Fur was removed from the chest by application of a cosmetic cream to gain a clear image.

Echocardiographic parameters were measured at the level of the papillary muscles in the parasternal short-axis view (M mode). LV fractional shortening was calculated as follows: $FS = ((LVEDD - LVESD) / LVEDD) \times 100$, where LVFS indicates LV fractional shortening; LVEDD, LV end-diastolic diameter; and LVESD, LV end-systolic diameter. LV ejection fraction was calculated automatically by the echocardiography system. All measurements were averaged on 5 consecutive cardiac cycles per experiment and cardiac function was assessed when heart rate was 450–500 bpm. Complete list of the heart parameters measured is reported in Table S2.

Glucose-tolerance and insulin-resistance tests

To determine fasting blood glucose levels, 1 mg/g glucose solution (D-Glucose; Sigma-Aldrich) was injected intraperitoneally into the mice after 16 hours fasting period. Blood glucose was measured from the tail vein immediately prior to glucose administration and after 20, 40 and 60 minutes with a glucometer (ACCU-CHEK Aviva blood glucose meter; Roche). To test insulin-tolerance mice were fasted for 16 hours, blood glucose was first measured from the tail vein, then the mice received an intraperitoneal injection of insulin (0.75 U/kg; Sigma-Aldrich) and blood glucose was measured again at time-points of 20, 50 and 80 minutes after injection. Evaluation of glucose tolerance and insulin resistance were performed B.I., 60, and 120 days after Au₈-pX injection.

Real-Time qPCR

For the quantitative analysis of mRNA expression, tissue fragments were freshly dissected from injected and the control (not injected) animals at the moment of sacrifice, immediately placed in Trizol Reagent (Roche) and extracted as indicated by the manufacturer. RNA quality, primer efficiency and correct product size were verified by RT-PCR and agarose gel electrophoresis. Real-Time qPCR was

performed with LightCycler (Roche) using FastStart DNA MasterPLUS SYBR-Green I (Roche). 2 µl of cDNA was used in each reaction. All samples were done in triplicates. Specificity and absence of primer dimers was controlled by denaturation curves; for each mRNA examined only one denaturation peak was observed. GAPDH was used for normalization, calculated using LightCycler Software 3.5.3. Primer sequences are reported in Table S1.

Biochemical Methods

Mitochondrial isolation

Tissues were dissected and immediately frozen by immersion in liquid N₂, then pulverized and stored at -80 °C. To isolate mitochondrial fractions, tissue powders were washed twice in ice-cold PBS, lysed in 0.5 ml mitochondria lysis buffer (50 mM Tris, 100 mM KCl, 5 mM MgCl₂, 1.8 mM ATP, 1 mM EDTA, pH 7.2), supplemented with protease inhibitor cocktail III (Calbiochem, La Jolla, CA, USA), 1 mmol/l PMSF and 250 mM NaF. The samples were clarified by centrifugation at 650 g for 3 minutes at +4 °C: the supernatant was collected and centrifuged at 13,000 g for 5 minutes at +4 °C. The supernatant, corresponding to the cytosolic fraction, was transferred into a new series of tubes. The pellet, containing mitochondria, was washed once with lysis buffer and resuspended in 0.25 ml of a resuspension buffer composed of 250 mM sucrose, 15 mM K₂HPO₄, 2 mM MgCl₂, 0.5 mM EDTA. A 50 µl aliquot was sonicated and used for the measurement of protein content or western blotting. To confirm the presence of mitochondrial proteins in the extracts, 10 µg of each sonicated sample were subjected to SDS-PAGE and probed with an anti-porin antibody (Abcam, Cambridge, UK).

ROS measurement

To measure total ROS, 100 µg proteins from tissue homogenates were re-suspended in 0.5 ml PBS, incubated for 30 minutes at 37°C with 5 µM of the fluorescent probe 5-(and-6)-chloromethyl-2',7'-

dichlorodihydro-fluorescein diacetate-acetoxymethyl ester (DCFDA-AM; Sigma Chemical Co.), centrifuged at 13,000 *g* at 37°C and re-suspended in 0.5 ml PBS. The fluorescence of each sample, considered an index of ROS levels, was read at 492 nm (λ excitation) and 517 nm (λ emission), using a HT Synergy 96-well micro-plate reader (Bio-Tek Instruments, Winooski, VT). The results were expressed as nmoles/mg tissue proteins. To measure mitochondrial ROS, 50 μ g proteins from mitochondrial extracts were stained with 5 μ M of DCFDA-AM, as reported above. The results were expressed as nmoles/mg mitochondrial proteins.

Lipoperoxidation and DNA oxidative damage

The 4-OH-nonenale, an index of lipid peroxidation, was measured on 100 μ g proteins from tissue homogenates or 50 μ g proteins from mitochondrial extracts using the Lipid Peroxidation (4-HNE) Assay Kit (Abcam). Results were expressed as nmoles/mg total or mitochondrial proteins. To evaluate 8-oxo-deoxy-guanosine, an index of DNA oxidative damage, we extracted 50 ng of DNA from tissue homogenates or 10 ng of DNA from mitochondrial extracts using the DNeasy Blood and Tissue Kit (Qiagen, Hilden, Germany). Samples were probed with the DNA/RNA Oxidative Damage ELISA Kit (Cayman Chemical, Ann Arbor, MI), as per manufacturer's instructions. Results were expressed as nmoles/ μ g total or mitochondrial DNA.

Glutathione and glutathione S transferase (GST) measurement

100 μ g proteins from tissue homogenates in 480 μ l PBS, were precipitated by adding 120 μ l of 6.5% w/v 5-sulfosalicylic acid. Each sample was placed in ice for 1 h and centrifuged for 15 minutes at 13,000 *g* (4°C). Total glutathione was measured in 20 μ l of the lysate with the following reaction mix: 20 μ l stock buffer (143 mM NaH₂PO₄ and 63 mM EDTA, pH 7.4), 200 μ l daily reagent (10 mM 5,5'-dithiobis-2-nitrobenzoic acid and 2 mM NADPH in stock buffer), 40 μ l glutathione reductase (8.5 U/ml). The content of oxidized glutathione (GSSG) was obtained after derivatization of GSH with 2-

vinylpyridine (2VP): 10 μ l of 2VP was added to 200 μ l of lysate, the mixture was shaken at room temperature for 1 hour. Glutathione was then measured in 40 μ l of sample as described. The reaction was followed kinetically for 5 minutes using a Synergy HT Multi-Mode Microplate Reader (Bio-Tek Instruments), measuring the absorbance at 415 nm. Each measurement was made in triplicate and results were expressed as pmoles glutathione/min/mg tissue proteins. For each sample, reduced glutathione (GSH) was obtained by subtracting GSSG from total glutathione. GST activity was measured using the Glutathione S-transferase (GST) assay kit (Sigma Chemicals. Co), as per manufacturer's instructions. Results were expressed as μ moles CDNB-GSH adducts/min/mg proteins.

Superoxide dismutase (SOD) measurement

The activity of cytosolic SOD1 and mitochondrial SOD2 was measured using 10 μ g of cytosolic and mitochondrial proteins, after the cytosol-mitochondrial separation obtained as detailed above. Samples, re-suspended into 100 μ l PBS, were incubated with 50 μ M xanthine, 5 U/ml xanthine oxidase, 1 μ g/ml oxidized cytochrome c for 5 minutes at 37°C. The rate of cytochrome c reduction, which is inhibited by the presence of SOD, was monitored for 5 minutes by reading the absorbance at 550 nm with a Packard microplate reader EL340 (Bio-Tek Instruments). Results were expressed as μ moles reduced cytochrome c/min/mg cytosolic or mitochondrial proteins.

Electron transport chain measurement

To measure the electron flux from complex I to complex III, taken as index of the mitochondrial respiratory activity, 50 μ g of proteins, derived from non-sonicated mitochondrial samples, were re-suspended in 0.2 ml of buffer A (5 mM KH_2PO_4 , 5 mM MgCl_2 , 5% w/v BSA) and transferred into a 96-well plates. Then 0.1 ml of buffer B (25% w/v saponin, 50 mM KH_2PO_4 , 5 mM MgCl_2 , 5% w/v BSA, 0.12 mM cytochrome c-oxidized form, 0.2 mM NaN_3) was added for 5 minutes at room temperature. The reaction was started with 0.15 mM NADH and was followed for 5 minutes, reading the absorbance

at 550 nm by a Packard microplate reader EL340 (Bio-Tek Instruments, Winooski, VT, USA). The results were expressed as nmoles of cytochrome c reduced/min/mg mitochondrial protein.

Mitochondrial ATP measurement

The amount of ATP in mitochondrial extracts was measured with the ATP Bioluminescent Assay Kit (Sigma-Aldrich), as per manufacturer's instruction. The results were expressed as nmoles/mg mitochondrial proteins.

Western Blot

Western Blot analysis was performed on 5 μ M, 10 μ M Au₈-pXs treated and untreated BMSCs^{FRDA#1}, BMSCs^{FRDA#2}, age matched BMSCs^{CTR#1} and BMSCs^{CTR#2} and tissues from Au₈-pXs treated and untreated YG8sR mice (cerebellum, *quadriceps* and hearts). Both cells and tissues were lysed in NP40 lysis buffer composed of 50mM Tris-HCl pH 8.8 (Eurobio Scientific), 1% IGEPAL CA-630 (MP Biomedicals), 150 mM NaCl (VWR) supplemented with complete protease inhibitor cocktail and phosSTOP (Roche) on ice for 30 minutes followed by centrifugation at 15000g at 4°C to pellet cell debris. Supernatants were quantified according to Bradford protein assay using Coomassie Plus Protein Assay Reagent (Thermo Fisher Scientific) and Glomax Discover Microplate Reader; 40 μ g of total protein extracts were loaded for each sample on polyacrylamide gels. Proteins were then transferred to nitrocellulose membranes (Bio-Rad) and blocked with 5% nonfat dry milk (Bio-Rad) diluted in TBS (50 mM Tris-HCl, 150 mM NaCl pH 7.6) with 0.05% Tween 20 (Sigma-Adrich) for 1 hour at room temperature. Filters were incubated with primary antibodies overnight 4°C on mild shaking. List of antibody and dilutions used: anti-Frataxin (Abcam 1:500), anti-NFS1 (Santa Cruz Biotechnology 1:500), anti-NRF2 (Thermo Fisher Scientific 1:500), anti-LC3B (Sigma-Aldrich 1:500), anti-p62/SQSTM1 (Sigma-Aldrich 1:500), anti-ATG7 (Sigma-Aldrich 1:500), anti-PGC1 α (Santa Cruz Biotechnology

1:500), anti-PPAR- γ (Abcam 1:500), anti-Calbindin D-28K (EMD-Millipore 1:500), anti-Parvalbumin (Abcam 1:500), anti-DRP1 (Abcam 1:500), anti-Mitofusin1 (Abcam 1:500), anti-TRAF6 (Santa Cruz Biotechnology 1:500), anti-MMP-9 (Santa Cruz Biotechnology 1:500), anti-Collagen VI (Abcam 1:500), anti-Actin (Sigma-Aldrich 1:800), anti-Vinculin (Thermo Fisher Scientific 1:800). IgG-horseradish peroxidase (HRP)-conjugated secondary antibodies (1:3000, DakoCytomation) were used for detection. Images were acquired with Odyssey Imaging System (Li-COR Biosciences). Densitometry band quantifications were performed using ImageJ software (<http://rsbweb.nih.gov/ij/>).

Tissue preparation for TEM

For ultrastructural studies small tissue fragments (less than 2 mm²) were dissected and transferred in a fixative solution containing 2.5% glutaraldehyde (GA) in 0.1M cacodylate buffer (pH 7.4) for 24 hours and then transferred into 0.5% GA in cacodylate buffer. Samples were stored at +4 °C until used. Tissues were then post-fixed in 2% OsO₄ in 0.1 M cacodylate buffer (pH 7.4) for 1 hour, dehydrated in a graded series of ethanol and embedded in Epon resin. Examination was done on semithin sections stained with lead citrate and uranyl acetate with a transmission electron microscope (EM 109; Zeiss).

Detection of metal gold in Au₈-pXs treated YG8sR tissues

To verify the cluster circulation and the penetration into murine tissues, 12 months-old YG8sR mice (n=6) were injected with 10 μ M Au₈-pXs into the tail vein. Age matched YG8sR mice (n=6) were used as controls. Animals were sacrificed after 30 days (n=3 per experimental group) or 180 days (n=3 per experimental group) and the gold content was evaluated by an inductively coupled plasma mass spectrometry (ICP-MS). Experiments were performed by investigators blinded to animal group assignment. Selected tissues were collected for analysis: heart, brain cortex and cerebellum, basal

ganglia, muscles (i.e. *quadriceps*, *tibialis anterior*, and *soleus*), liver, lung, kidney and pancreas. An amount of approximately 0.03 g of tissues was subjected to extractive mineralization using a Milestone Microwave LabSystem (Milestone, Sorisole (BG) – Italy) with a mixture of 8 ml of 65% aqueous nitric acid and 2 ml of 30% aqueous H₂O₂. The final volume was 12.5ml. The digestion took place in a Parr bomb (Milestone SK-10 High Pressure Rotor) at a temperature of 200 °C for 30 '. The microwave oven power was 1500 W. The ICP- MS analysis was performed with a Thermo iCAP Q instrument (Thermo Scientific, Rodano (MI) - Italy) with a quadrupolar analyzer. Argon was used for plasma at 15 ml/min and as atomizing gas at 1 L/min. RF power was 1.55 kW. Calibration was performed with Au from multielement standard solution for ICP (Sigma-Merck, Milan, Italy) in the range 0.3-100 ng/ml. Limit of quantification was 0.3 ng/ml.

In vivo imaging

12 months old Au₈-pXs treated and untreated YG8sR mice (n=3 mice per group) were anesthetized by intraperitoneal injections of Pentobarbital (1 ml per 100 g body weight); depth of anaesthesia was tested by the absence of reflexions after a painful stimulus. During surgery, the body temperature was maintained at 37°C with a thermostatically controlled warming pad (Harvard Apparatus). After shaving the skull and its fixation in a stereotactic frame (Stoelting Europe, Dublin, IRL), the scalp was lifted with forceps and opened by surgical scissors. Within the surgical area, the periosteum was removed from the surface of the skull to prepare the cranial window over the parietal cortex located between -2 mm and -6 mm in relation to the Bregma, and 1 mm to 5 mm lateral in relation to the sagittal suture. After surgery the cranial window was filled with sterile irrigation (e.g. sodium chloride 0,9%) and sealed by a 7 mm cover glass using the instant glue Roti-coll 1 (Carl Roth, Karlsruhe, GER). The in vivo imaging was performed with the Confocal Laser Leica SP8. To image cerebral blood

vessels, tail vein was cannulated and injected with antibody against CD31 fluorescently labeled with FITC (Thermo Fisher Scientific). For imaging, the mouse skull was fixed in a head holder and the animal was placed on a heating plate under the microscope for one imaging session. The known maximum achievable depth for in vivo imaging in mouse using this approach is $\leq 200 \mu\text{m}$.

Supplementary Figure legends

Supplementary Fig.1

A) Bright field images and FACS analysis of BMSCs derived from FRDA patients. Scale bars, $75\mu\text{m}$. BMSCs were tested for mesenchymal marker expression CD73, CD90 and CD105.

B) Proliferation of $\text{BMSCs}^{\text{FRDA}\#1}$, $\text{BMSCs}^{\text{FRDA}\#2}$ and $\text{BMSCs}^{\text{CTR}}$ was evaluated for 72 hours with MTT assay.

C) Basal and maximal respiratory capacity, spare capacity and non-mitochondrial respiration was evaluated in $\text{BMSCs}^{\text{FRDA}\#1}$ and $\text{BMSCs}^{\text{CTR}}$ through XFp Seahorse Mito Stress Kit.

B-C Means \pm SD (n=3 independent experiments) * $P < 0.05$, ** $P < 0.01$, *** $P < 0.001$, **** $P < 0.0001$ (ordinary two- way ANOVA- Bonferroni's test).

Supplementary Fig.2

A) Evaluation of the gold content in $\text{Au}_8\text{-pX}$ YG8sR tissues through a coupled plasma mass spectrometry (ICP-MS) analysis. $\text{Au}_8\text{-pX}$ -injected YG8sR mice were sacrificed at early (30 days; n=3) and late (180 days; n=3) time points. Not injected YG8sR mice were used for comparative analysis for each time point (30 days, n=3; 180 days, n=3). Data were expressed as Means \pm SD (ordinary two- way ANOVA- Bonferroni's test). Gold content within SL fell below the detection limit of the instruments.

B) Representative in vivo confocal image montage of Au8-pXs circulating in brain vessels of Au8-pX YG8sRs mice and migrating to surrounding tissues (in gray-pseudocolor). Vessels were stained by anti-CD31FITC antibody (in blue- pseudocolor).

Supplementary Fig.3

A, B) Western Blot quantifications of frataxin and FXN related proteins (Nrf2, NFS1, PGC-1 α and PPAR γ), proteins related to the autophagic flux (LC3I, LC3II, p62, and Atg7) and marker of fibrosis (ColVI, MMP9 and TRAF6) in Au8-pX YG8sR and YG8sR hearts (**A**) and QAs (**B**). Vinculin was used as loading control. Data were expressed as Means \pm SD (n=2-4 independent experiments); * P< 0.05, ** P<0.01, *** P<0.001, **** P<0.0001 (ordinary one- way ANOVA- Bonferroni's test).

Supplementary Fig.4

Western Blot quantifications of frataxin and FXN related proteins (Nrf2, NFS1, PGC-1 α and PPAR γ), proteins related to the autophagic flux (LC3I, LC3II, p62, and Atg7) and Purkinje cells (Parvalbumin and Calbindin-D) in Au8-pX YG8sR and YG8sR cerebellum. Vinculin was used as loading control. Data were expressed as Means \pm SD (n=2-4 independent experiments); * P< 0.05, ** P<0.01, *** P<0.001, **** P<0.0001 (ordinary one- way ANOVA- Bonferroni's test).

Supplementary Fig.5

A) Glucose tolerance test: blood glucose levels in Au8-pX YG8sR and YG8s mice fasted for 16 hours after intraperitoneal administration of glucose.

B) Insulin resistance test: blood glucose levels in Au8-pX YG8sR and YG8s mice fasted for 16 hours after intraperitoneal injection of insulin.

A-B Data were expressed as Means \pm SD (n=5 mice per group); ordinary two-way ANOVA-Bonferroni's.

Supplementary Tables

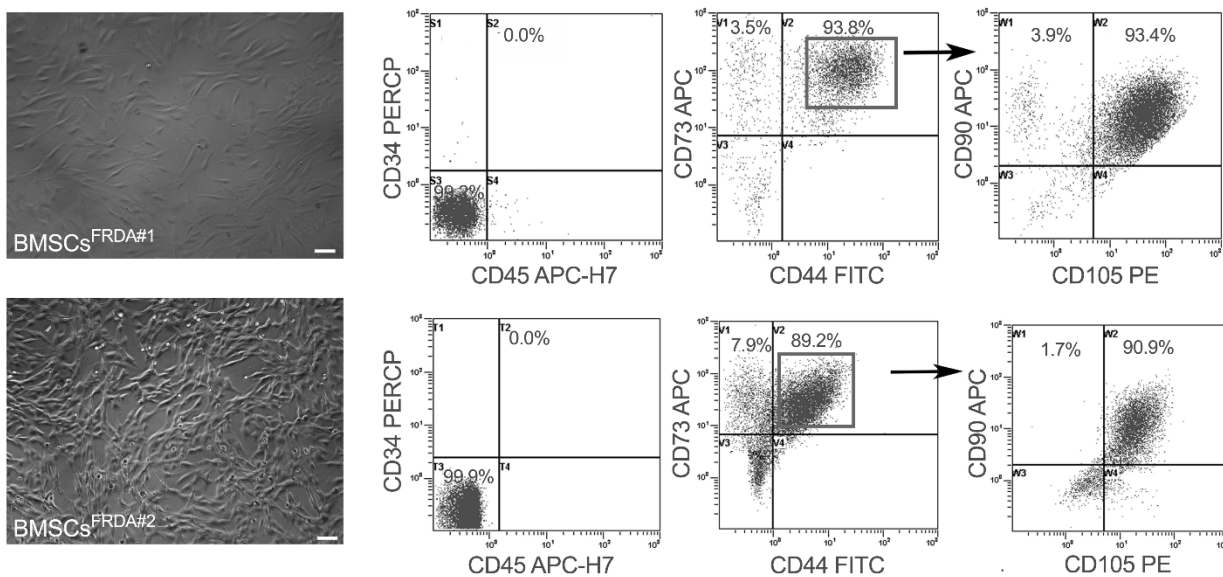
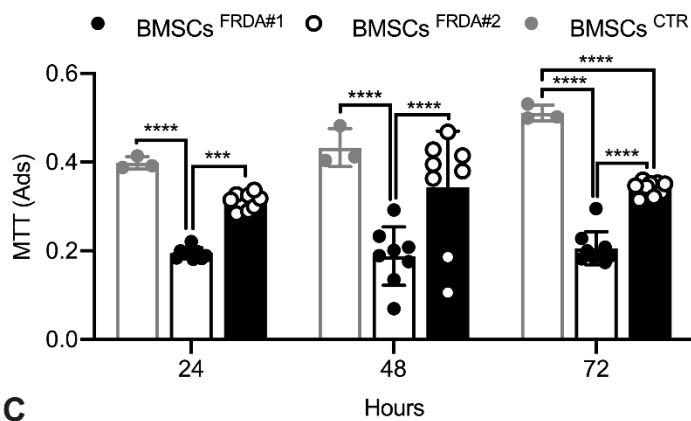
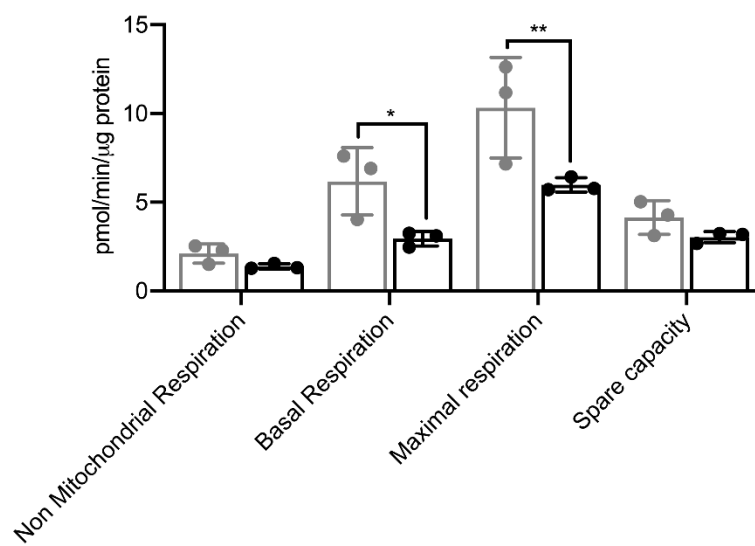
Table S1. Primer list.

Gene Name	Primer Sequence	Species	Use
<i>Fxn fw</i>	CTTCCCTCTACCCTGCCTTC	mouse	Genotyping
<i>Fxn rv</i>	GGAGAACAGTGGACACAGTAACA	mouse	Genotyping
<i>Fxn fw</i>	GGGCAGATAAAGGAAGGAGATAC	human	Genotyping
<i>Fxn rv</i>	ACGATAGGGCAACACCAATAA	human	Genotyping
<i>Nrf2 fw</i>	TTTTCCATTCCCGAATTACAGT	mouse	RT-qPCR
<i>Nrf2 rv</i>	GGAGATCGATGAGTAAAAATGGT	mouse	RT-qPCR
<i>Prdx2 fw</i>	GGCAACGCGCAAATCGGAAAAG	mouse	RT-qPCR
<i>Prdx2 rv</i>	TCCAGTGGGTAGAAAAAGAGGA	mouse	RT-qPCR
<i>Gstm1 fw</i>	CCTATGATACTGGGATACTGGAACG	mouse	RT-qPCR
<i>GStm1 rv</i>	GGAGCGTCACCCATGGTG	mouse	RT-qPCR

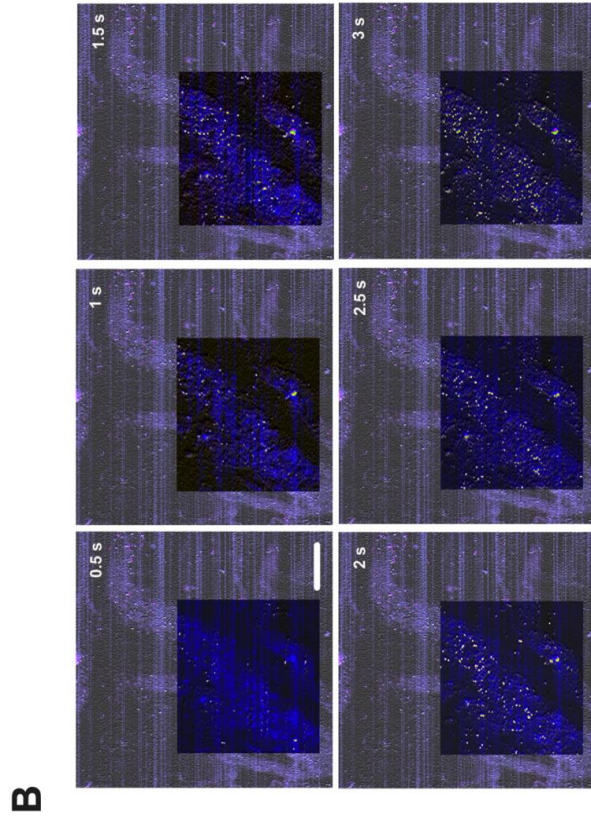
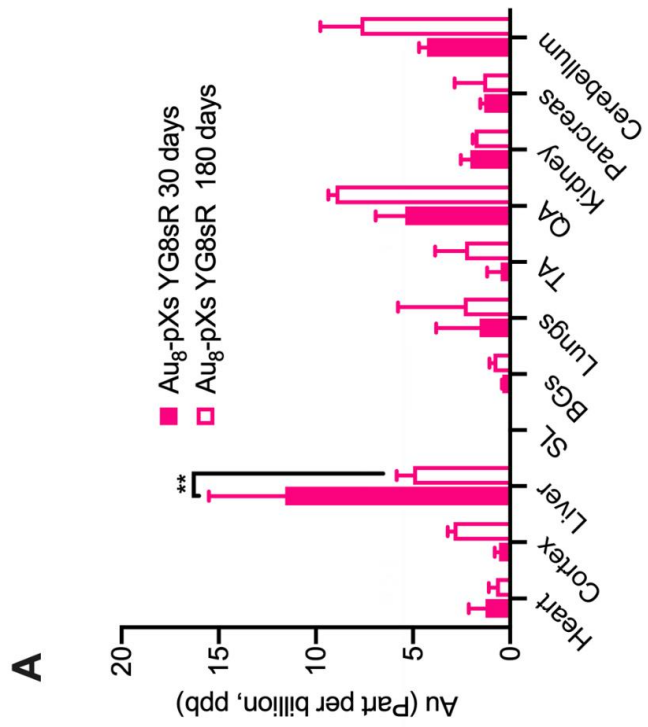
Table S2. Heart Parameters

Heart Parameters		Units
AV Peak Pressure	Aortic Valve -Peak Pressure	mmHg
AVA	Aortic Valve -Area	mm ²
LVOT CO	Left Ventricular Outflow Tract -Cardiac Output	μl/min
LVOT SV	Left Ventricular Outflow Tract -Stroke Volume	μl
MV Area (simplified)	Mitral Valve Area	mm
RVOT	Right Ventricular Outflow Tract	mm
RVOT SV	Right Ventricular Outflow Tract -Stroke Volume	mm
RVOT CO	Right Ventricular Outflow Tract -Cardiac Output	mm
IVS d	Intraventricular Septum Thickness at end-diastole	mm
IVS s	Intraventricular Septum Thickness at end-systole	mm
LVID d	Left Ventricular internal dimension at end-diastole	mm

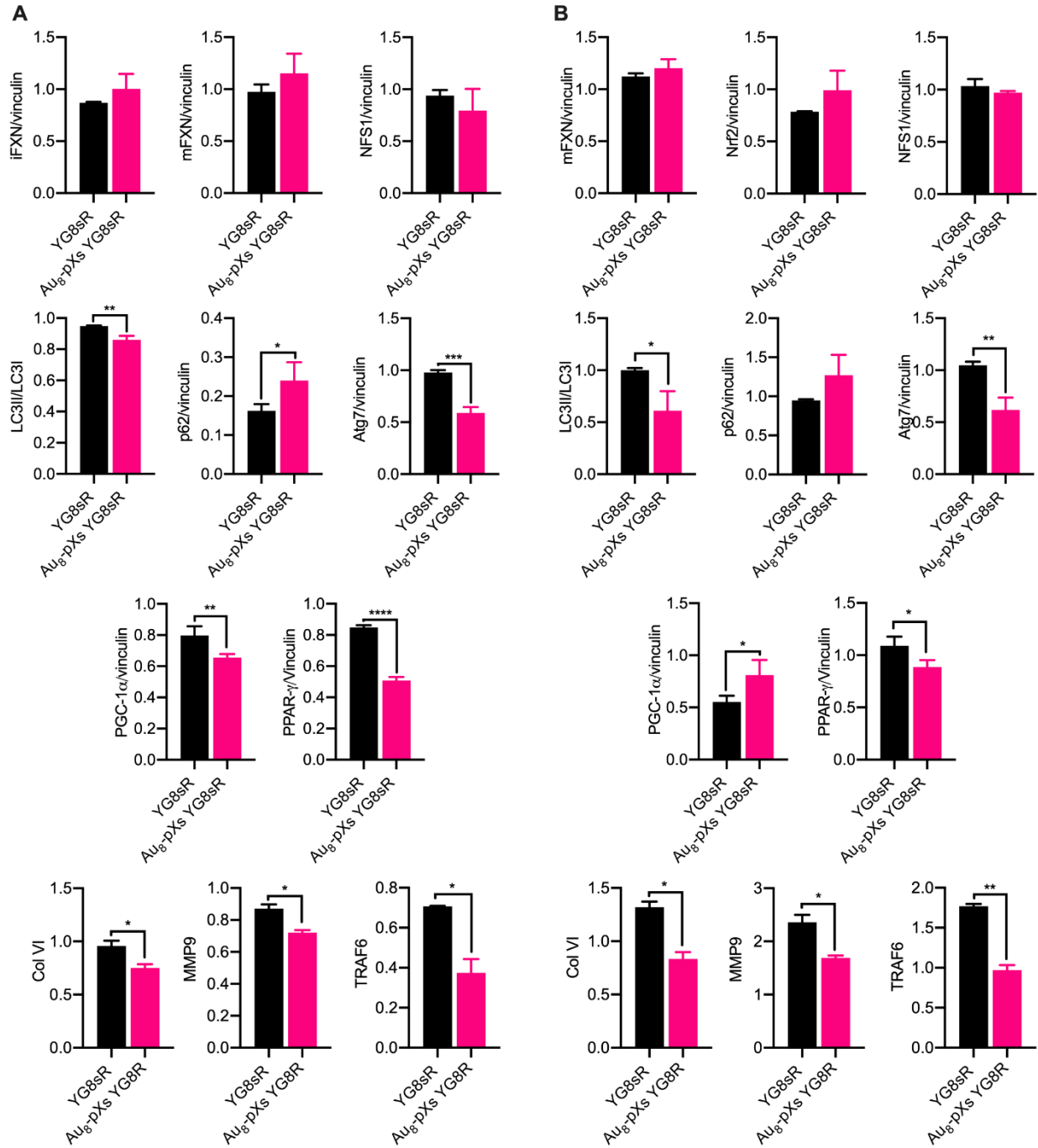
LVID s	Left Ventricular Internal Dimension at end-systole	mm
LVPW d	Left Ventricular Posterior Wall Thickness at end- diastole	mm
LVPW s	Left Ventricular Posterior Wall Thickness at end-systole	mm
LV Mass	Left Ventricular Mass	mg
LV Vol d	Left Ventricular Volume at end-diastole	μl
LV Vol s	Left Ventricular Volume at end-systole	μl

A**B****C**

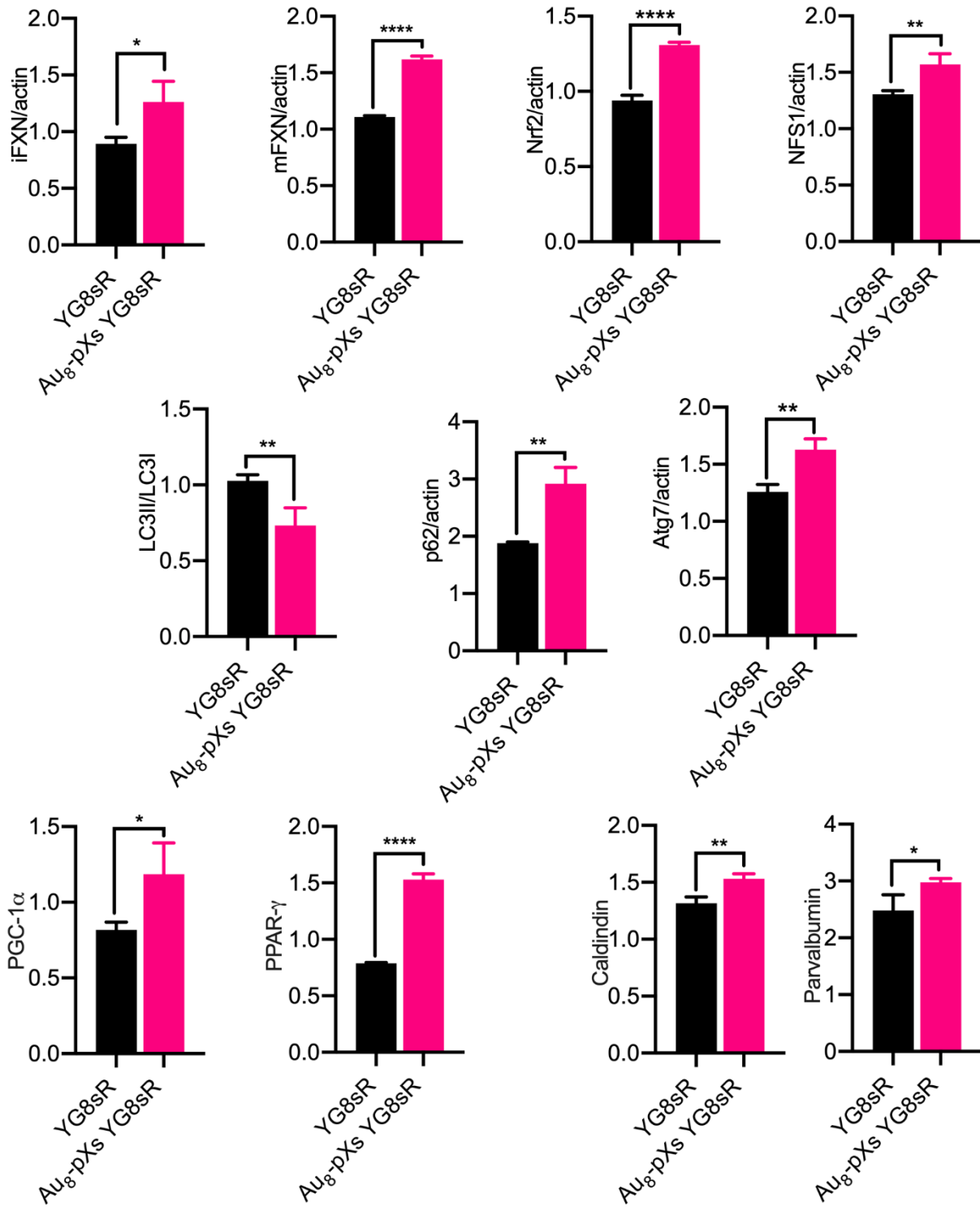
Supplementary Figure 1



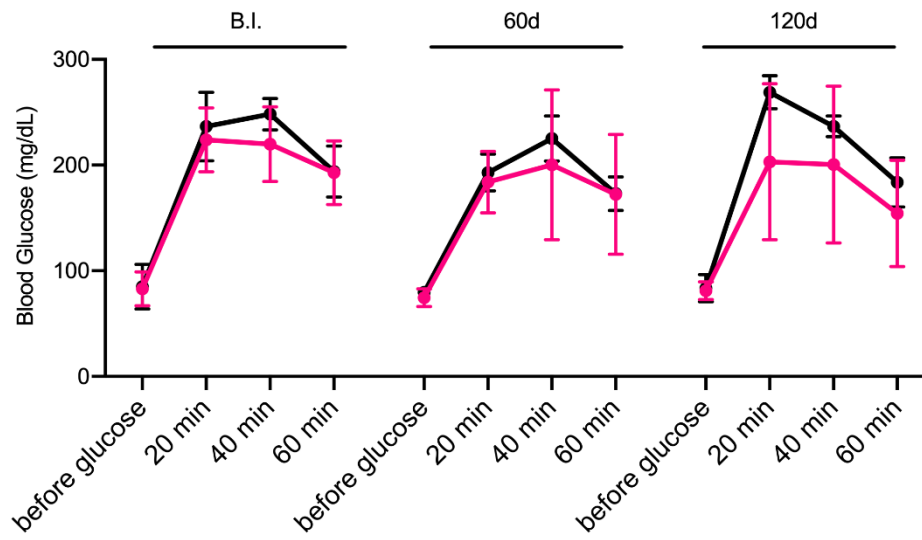
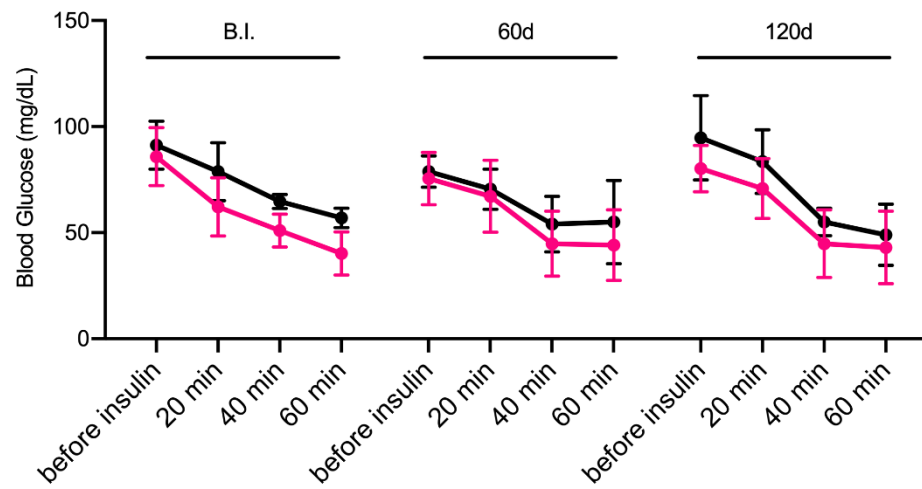
Supplementary Figure 2



Supplementary Figure 3



Supplementary Figure 4

A**B****Supplementary Figure 5**